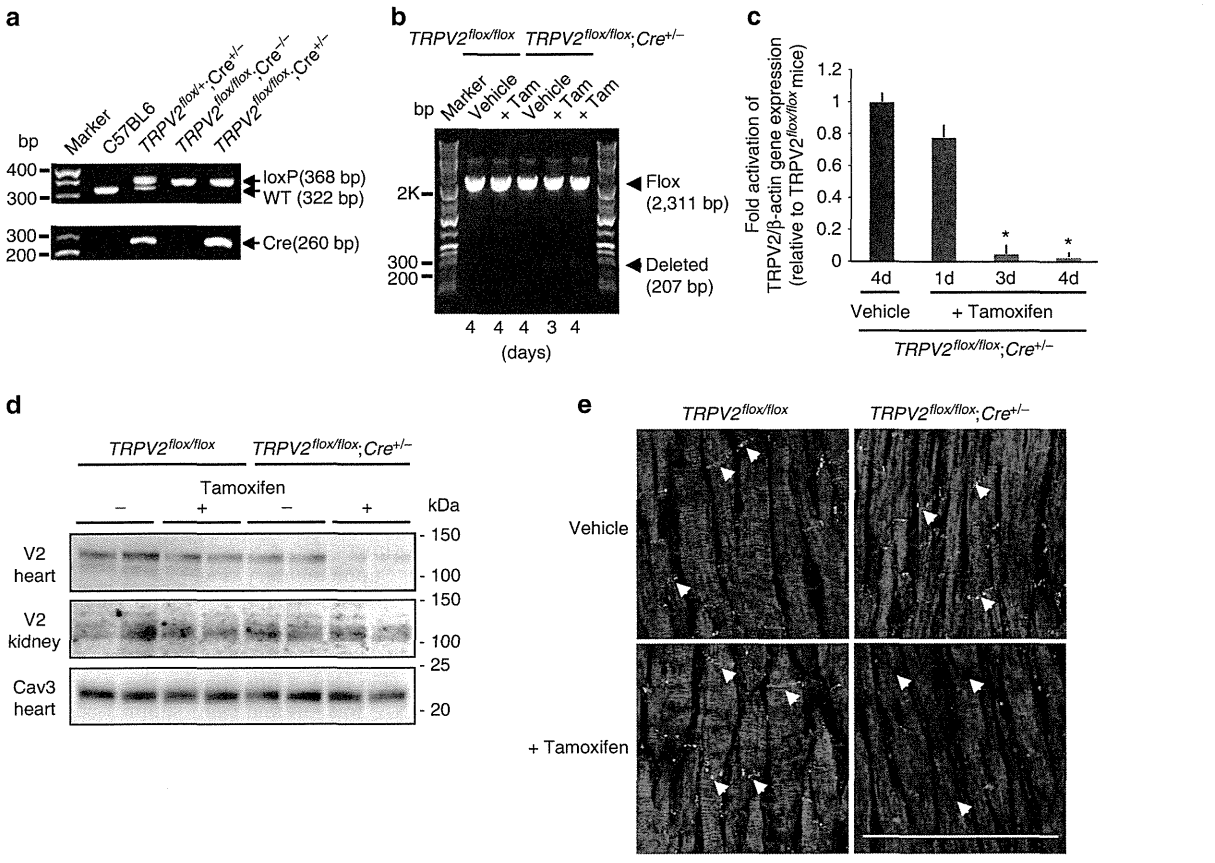

Figure 1 | Generation of temporally controlled cardiac-specific TRPV2-deficient mice. (**a**) Genotyping of *TRPV2*$^{flox/flox}$;*MerCreMer*$^{+/-}$ mice using tail genomic DNA. (**b**) Confirmation of *Cre* recombination by PCR of cardiac genomic DNA. (**c**) TRPV2 messenger RNA expression confirmed by RT-PCR, using β-actin as an internal control gene ($n=3$ mice per group). Data are mean ± s.e.m. *$P<0.05$ versus non-treated age-matched *TRPV2*$^{flox/flox}$; *MerCreMer*$^{-/-}$ (*TRPV2*$^{flox/flox}$) mice. (**d**) Expression of TRPV2 protein in heart and kidney from tamoxifen-treated and -untreated *TRPV2*$^{flox/flox}$ or *TRPV2*$^{flox/flox}$;*MerCreMer*$^{+/-}$ (*TRPV2*$^{flox/flox}$; *Cre*$^{+/-}$) mice, using caveolin 3 as an internal control for hearts. Membrane extracts (10 μg per lane) were subjected to immunoblotting. (See full blots with marker position in Supplementary Fig. 6). (**e**) Triple staining of left ventricle sections with anti-TRPV2 antibody (green), phalloidin (red) and DAPI (blue). Scale bar, 100 μm. Arrows, intercalated discs.

mice died within 10 days of the onset of tamoxifen treatment, suggesting an indispensable role for TRPV2 in the working heart (Fig. 2f).

The cardiovascular function in TRPV2-deficient mice. Echocardiography revealed a severe decline in fractional shortening and an increased left ventricular diastolic dimension 4 days after the start of tamoxifen treatment (Fig. 3a,b). Cardiac dysfunction was not observed in tamoxifen-treated *TRPV2*$^{flox/+}$; *MerCreMer*$^{+/-}$ mice (hetero knockout (KO) mice) for 4 days (Supplementary Fig. 2). Therefore, the cardiac dysfunction seen in TRPV2-deficient mice (homo KO mice) is not due to side effects associated with the overexpression of *Cre* recombinase or tamoxifen administration.

Figure 3c,d show that aortic blood pressure also gradually dropped in TRPV2-deficient mice after 3 days of tamoxifen treatment, although the heart rate did not change (Fig. 3e). Notably, the time course of blood pressure decline closely paralleled the time course of *Cre-loxP* recombination in tamoxifen-treated *TRPV2*$^{flox/flox}$;*MerCreMer*$^{+/-}$ mice (Fig. 1b,c). Therefore, the rapid reduction in blood pressure appeared to result from the severe decline in cardiac pump function following the elimination of TRPV2. This suggests that TRPV2 is critical for cardiac function under basal conditions.

The disordered intercalated discs in TRPV2-deficient hearts. Although the gross morphology of the hearts of tamoxifen-treated *TRPV2*$^{flox/flox}$;*MerCreMer*$^{+/-}$ mice after 4 days was effectively normal (Fig. 2a), the ultrastructure of the intercalated discs was already dramatically disrupted (Fig. 4a), showing extensive interdigitation, irregular shapes, lacunae and widened spaces at the sites of myofibril attachment. Immunostaining for N-cadherin and β-catenin, components of adherens junctions[4–6], showed a denser localization at cell–cell interfaces in TRPV2-deficient hearts compared with vehicle controls (Fig. 4b). The structural abnormality of intercalated disc architecture seen in *TRPV2*$^{flox/flox}$; *MerCreMer*$^{+/-}$ hearts is considered synonymous with impaired mechanical interactions with neighbouring myocytes[15]. These observations suggest that the severe decline in cardiac pump function was associated with the structural disruption of intercalated discs and adherens junctions, suggesting that mechanical coupling at these sites is under the control of TRPV2.

TRPV2 elimination affects myocardial electrical coupling. A number of cardiac disorders have been described in which disruption of the intercalated disc structure significantly affects electrical coupling[4]. In TRPV2-deficient myocytes, 4 days after the onset of tamoxifen treatment, the gap junction protein connexin 43 showed diffuse localization in the intercalated discs

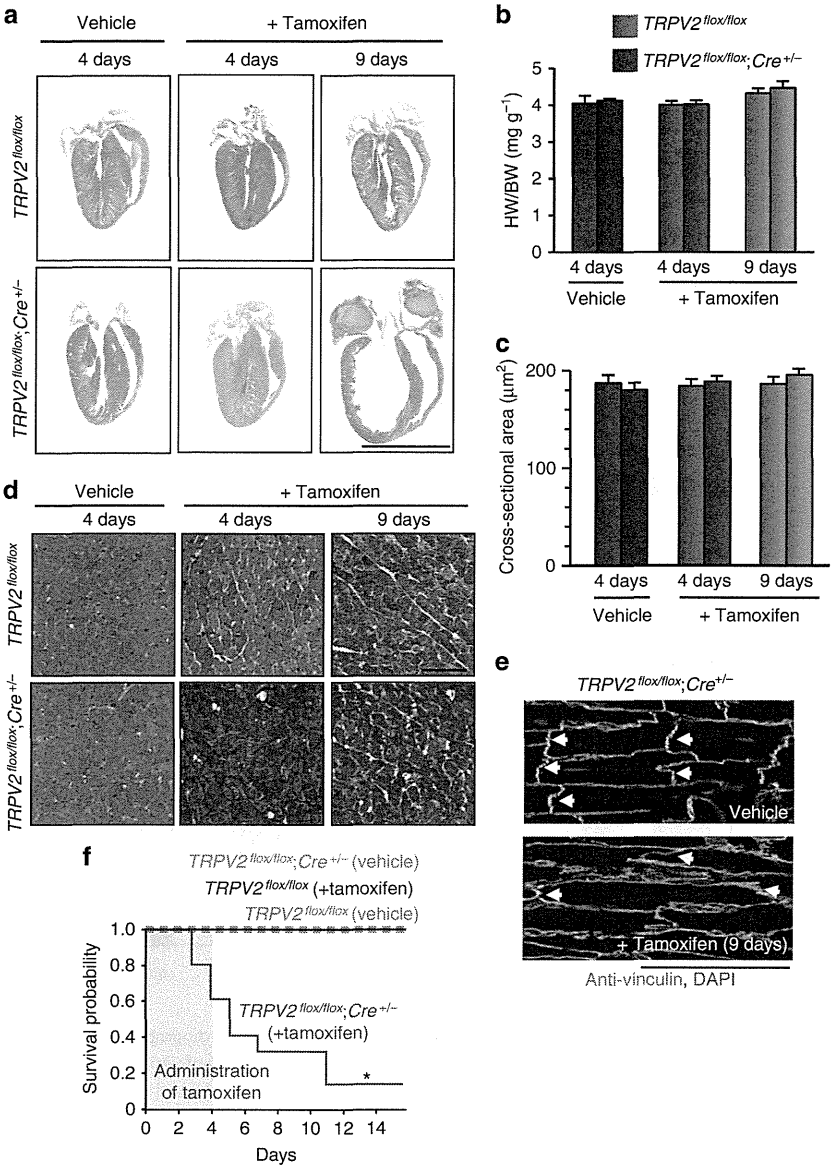

Figure 2 | Morphological changes and survival in TRPV2-deficient mice. *TRPV2*$^{flox/flox}$;*MerCreMer*$^{-/-}$ (*TRPV2*$^{flox/flox}$) and *TRPV2*$^{flox/flox}$;*MerCreMer*$^{+}$ (*TRPV2*$^{flox/flox}$;*Cre*$^{+/-}$) mice, treated with tamoxifen or vehicle, were analysed on day 4 and day 9. (**a**) Cardiac morphology. Scale bar, 5 mm. (**b**) Heart weight (HW)/body weight (BW) ratio. Data are mean ± s.e.m. ($n = 22$–35 hearts per group) (**c**) Cross-sectional areas from paraffin sections of left ventricles. Data are mean ± s.e.m. ($n = 122$–153 cells from three hearts per group) (**d**) Masson's trichrome staining of the left ventricle. Scale bar, 50 μm (**e**) Double staining with anti-vinculin antibody (green) and DAPI (blue). Scale bar, 100 μm. Arrowheads, intercalated discs. (**f**) Survival probabilities ($n = 55$–85 per group). *$P < 0.05$ versus *TRPV2*$^{flox/flox}$;*Cre*$^{+/-}$ mice treated with vehicle, by log-rank tests.

and its expression spread along the sarcolemma over time (Fig. 5a). Typical electrocardiograms obtained by telemetry showed no abnormalities over the first 4 days of tamoxifen administration (Fig. 5b); however, after 5 days, QRS complexes time-dependently widened (Supplementary Fig. 3), and 1 week after the onset of tamoxifen treatment, TRPV2-deficent hearts showed intraventricular conduction delays (Fig. 5b). As this phenomenon occurred several days after a drop in blood pressure was seen (Fig. 3c), it is likely that the disorganization of the intercalated disc architecture after the loss of TRPV2 had an indirect effect on electrical coupling with neighbouring myocytes.

TRPV2-deficient cardiomyocytes are fully functional. Abnormal Ca^{2+} handling by cardiomyocytes is a central cause of contractile dysfunction[3]. To investigate the E–C coupling of TRPV2-deficient myocytes, we analysed contractility and Ca^{2+} handling in single cardiomyocytes from tamoxifen-treated and -untreated *TRPV2*$^{flox/flox}$;*MerCreMer*$^{+/-}$ mice. Despite severe cardiac dysfunction, single myocytes isolated from these mice treated with tamoxifen for 4 days showed no abnormalities in cell morphology and shortening (Fig. 6a,b) or intracellular Ca^{2+} transients evoked by electrical stimulation (Fig. 6c), suggesting that the ablation of TRPV2 causes no significant change in intracellular Ca^{2+} handling for E–C coupling. By contrast, after 9 days of tamoxifen treatment, the isolated TRPV2-deficient cardiomyocytes showed an elongated morphology (Fig. 6a). These myocytes showed significantly impaired contractility (Fig. 6b) and Ca^{2+} cycling (Fig. 6c), compared with vehicle-treated control cells, and electrically evoked Ca^{2+} transient peaks

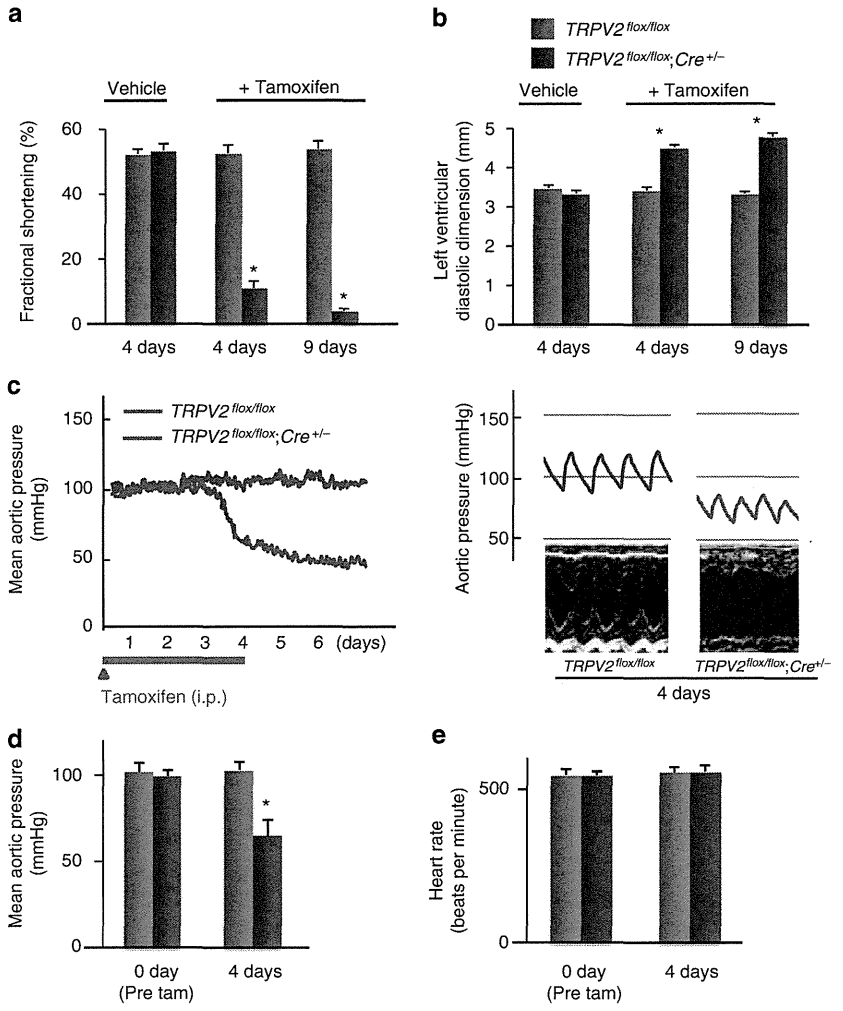

Figure 3 | Rapid, severe decline in cardiac pump function after TRPV2 elimination. (**a**,**b**) Echocardiographic parameters ($n=5$ per group). Data are means ± s.e.m. *$P<0.05$ versus *TRPV2*$^{flox/flox}$;*Cre*$^{+/-}$ mice treated with vehicle, by two-way analysis of variance (ANOVA) with Bonferroni's *post hoc* test. (**c**) Representative pressure recording (left panel), and example of a pressure recording (upper right) and an echocardiograph (lower right) after tamoxifen treatment. (**d**,**e**) Mean aortic pressure and heart rate ($n=3$ per group). Data are means ± s.e.m. *$P<0.05$ versus all other groups, by one-way ANOVA with Bonferroni's *post hoc* test.

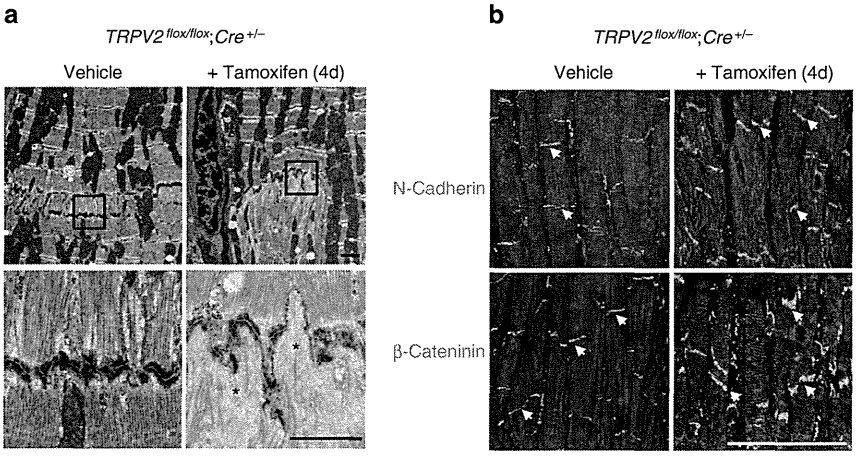

Figure 4 | Disorganization of intercalated discs in TRPV2-deficient hearts. (**a**) Electron micrographs of intercalated discs. Scale bar, 1 μm. Areas in black squares are magnified in lower panels. Asterisks, lacunae in intercalated discs. (**b**) Localization of N-cadherin and β-catenin in tamoxifen-treated *TRPV2*$^{flox/flox}$;*Cre*$^{+/-}$ mouse hearts. Scale bar, 75 μm. Arrows, intercalated discs.

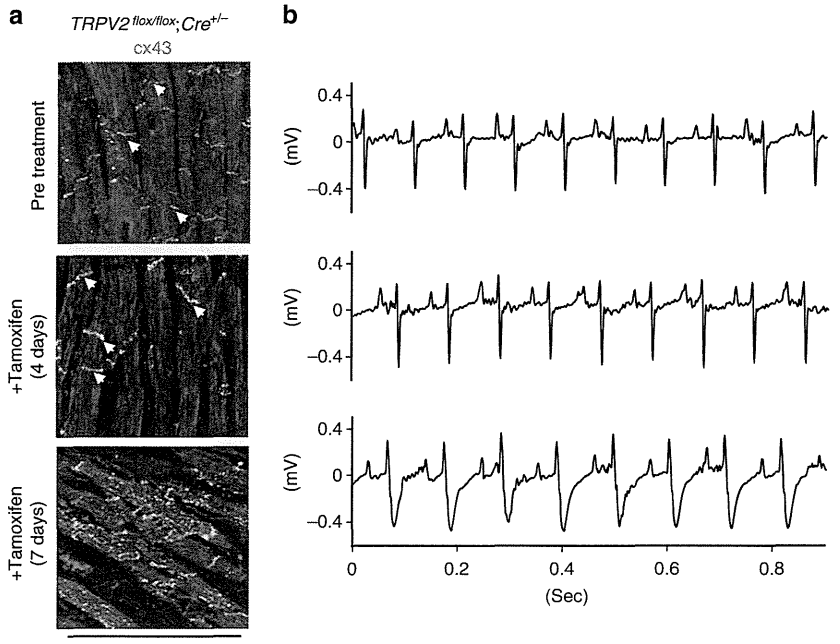

Figure 5 | Cardiac conduction defects after TRPV2 elimination. (**a**) Change in connexin 43 localization in *TRPV2*$^{flox/flox}$;Cre$^{+/-}$ hearts after tamoxifen treatment. Scale bar, 100 μm. (**b**) Intraventricular conduction delay after TRPV2 depletion. Electrocardiographs (comparable with lead II) obtained by telemetry.

with reduced amplitude and a slow decay speed (Fig. 6d,e). In addition, the Ca^{2+} content of the myocyte sarcoplasmic reticulum was reduced (Fig. 6f), although intracellular free Ca^{2+} concentrations under basal conditions were in line with the controls.

The subcellular structure of cardiomyocytes and the localization of Ca^{2+} regulatory proteins are well suited to their cellular functions[21]. In cardiomyocytes, Ca^{2+} release for contraction occurs at distinct structures (dyads) along T-tubules, which are critical for efficient E–C coupling[22]. In the dyad space in control vehicle-treated hearts, L-type Ca^{2+} channels and Na^{+}/Ca^{2+} exchangers were localized in T-tubules, and ryanodine receptors were located on sarcoplasmic reticulum membranes, so that these immunofluorescence signals appeared as well-ordered patterns (Fig. 7a). In *TRPV2*$^{flox/flox}$;*MerCreMer*$^{+/-}$ mice treated with tamoxifen for 4 days, the key Ca^{2+} regulatory proteins in cardiomyocyte E–C coupling (that is, L-type Ca^{2+} channels, ryanodine receptors, and Na^{+}/Ca^{2+} exchangers) were normally expressed, and localized in T-tubules and sarcoplasmic reticulum membranes, as in vehicle controls, suggesting normal Ca^{2+} handling in the cardiomyocytes (Fig. 7a,b). The myofilament structures were normal in these tamoxifen-treated mice for 4 days (Fig. 7c). Thus, the main cause of the rapid and severe decline in cardiac pump function in TRPV2-deficient hearts was not abnormal Ca^{2+} handling affecting myocyte E–C coupling or disorganization of contractile filaments.

Abnormal Ca^{2+} handling in TRPV2-deficient myocytes. In *TRPV2*$^{flox/flox}$;*MerCreMer*$^{+/-}$ hearts, 9 days after the onset of tamoxifen treatment the subcellular localization of L-type Ca^{2+} channels, ryanodine receptors and Na^{+}/Ca^{2+} exchangers was abnormal, representing a defect in intracellular Ca^{2+} handling (Fig. 7a), although the levels of expression of these Ca^{2+} regulatory proteins were similar to controls (Fig. 7b). It was possible that T-tubules and dyad structures were disordered in TRPV2-deficient hearts by day 9. In isolated cardiomyocytes at this stage, RyR activity was not only significantly lower (Fig. 6c,d), but the reaction area of Ca^{2+} sparks elicited by electrical stimulation was also reduced and showed subcellular heterogeneity (Supplementary Fig. 4). TRPV2-deficient myocytes on day 9 also showed extensive disorganization of the myofilaments needed to generate force (Fig. 7c). At this later stage, TRPV2-deficient myocytes showed impaired Ca^{2+} handling (Fig. 6b–f and Supplementary Fig. 4) and disorganization of the contractile cytoskeletal apparatus (Fig. 7c). Thus, eliminating TRPV2 not only led to a rapid and severe decline in normal cardiac pump function, but also resulted in a subsequent cellular dysfunction in individual myocytes.

Characterization of TRPV2-deficient neonatal cardiomyocytes. Intra-, inter- and extracellular mechanical forces play vital roles in the differentiation and maturation of cardiomyocytes, both in *in vivo* and *in vitro*[1–3]. In particular, the formation of mature intercalated discs is important during development for directing myofibrogenesis, appropriate Ca^{2+} handling for E–C coupling and differentiation into synchronously beating myocytes[6]. In cultured newborn cardiomyocytes, we were able to follow the formation of intercalated discs and the reorganization of myofibrils with time in myocytes isolated by enzymatic dissociation from neonatal heart tissue[23]. When we examined the formation of intercalated discs in cultured neonatal cardiomyocytes, by staining for the gap junction protein, connexin 43, and N-cadherin (Fig. 8a, upper and middle, first three panels), we observed that the intercalated disc structures at cell–cell interfaces showed many zigzags, sharp turns and a high degree of convolution. In control cardiomyocytes isolated from *TRPV2*$^{flox/flox}$;*MerCreMer*$^{-/-}$ with or without tamoxifen treatment or *TRPV2*$^{flox/flox}$;*MerCreMer*$^{+/-}$ mice cultured without tamoxifen (Fig. 8a, all panels except for right column), we observed well-developed sarcomeres, typical localization of connexin 43 and N-cadherin to intercalated discs at cell–cell interfaces and synchronously beating myocytes. In these

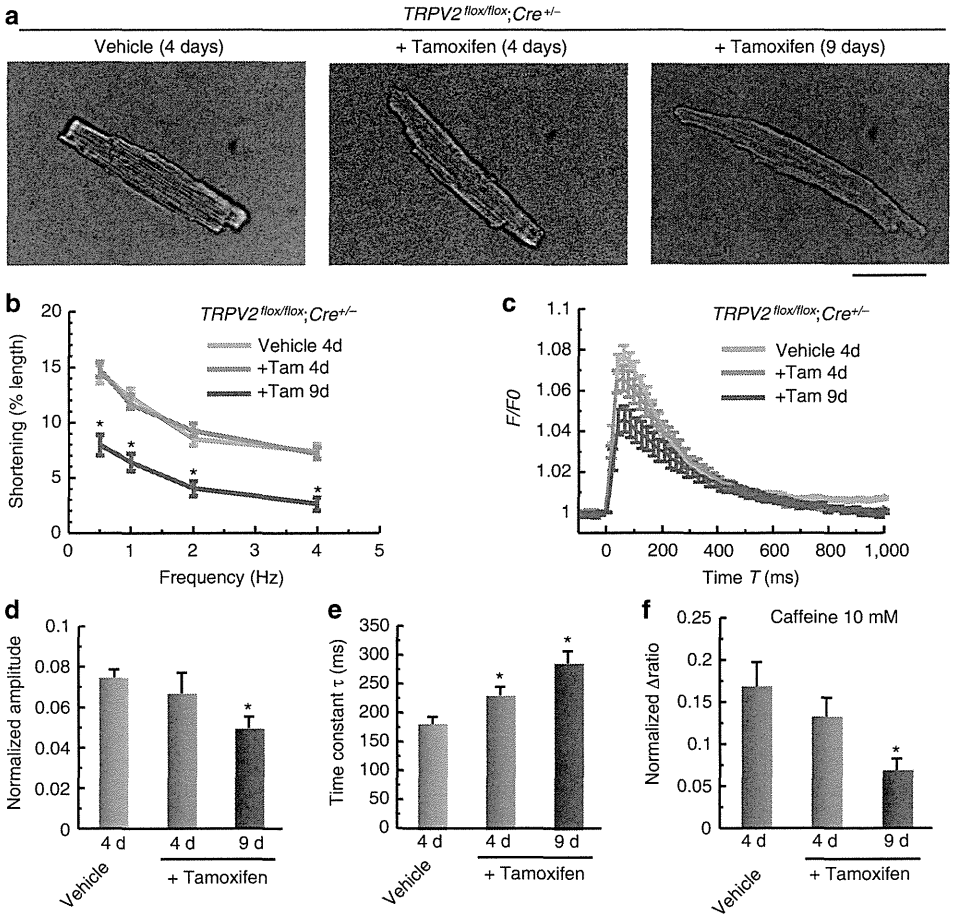

Figure 6 | Cardiomyocyte contractility and Ca^{2+} handling by isolated cells from TRPV2-deficient hearts. (**a**) Morphology of isolated cardiomyocytes. Scale bar, 50 μm. (**b**) Frequency-dependent shortening of myocytes ($n=100$, 175, and 58 cells measured from 8, 6 and 3 hearts). (**c**) Indo-1 fluorescence in single cardiomyocytes stimulated at 1 Hz ($n=28$, 18 and 12 cells from 7, 4 and 3 hearts). (**d**) Peak amplitude of Ca^{2+} transients. (**e**) Decay time constant obtained by fitting the decline phase. (**f**) Estimation of sarcoplasmic reticulum Ca^{2+} content. Data are means ± s.e.m. *$P<0.05$ versus vehicle control.

cardiomyocytes, NCX1 was highly expressed at the cell surface and at intercalated areas, indicating their maturation and differentiation into synchronously beating myocytes (Fig. 8a, first three bottom panels). By contrast, TRPV2-deficient myocytes cultured with 0.2 μg ml^{-1} tamoxifen for 48 h formed no intercalated discs between neighbouring cells, and showed aberrant intracytoplasmic accumulation of connexin 43, internally defuse N-cadherin, and reduced expression of NCX1 (Fig. 8a, right panels). Although we observed spontaneous weak beating in TRPV2-deficient myocytes, it was not synchronous.

Previously, we reported that recombinant TRPV2 in Chinese hamster ovary cells could be activated by stretch-induced mechanical stimulation[17,18]. We investigated whether neonatal cardiomyocytes showed an intracellular Ca^{2+} increase after stretch stimulation dependent upon TRPV2. In *TRPV2$^{flox/flox}$;MerCreMer$^{+/-}$* myocytes untreated with tamoxifen, an extracellular Ca^{2+}-dependent intracellular Ca^{2+} increase was detected after stretch stimulation, which was blocked by inhibitors of stretch-activated channels, Gd^{3+} or ruthenium red (RR) (Fig. 8b–d). Although RR is known to block RyR, its effect is not permanent, so using a bath application should limit its effects to plasma membrane channels[24]. By contrast, no stretch-evoked Ca^{2+} increase was observed in tamoxifen-treated myocytes. In addition, we confirmed the stretch-evoked Ca^{2+} increase in HEK293 cells expressing TRPV2 and the blockade of this response by Gd^{3+} or RR (Fig. 8e). These results indicate that TRPV2 is a key molecule in the stretch-induced Ca^{2+} response of cardiomyocytes. Interestingly, the formation of intercalated discs and the maturation into cardiomyocytes showing the synchronized beating and alignment of myofilaments seen in vehicle-treated *TRPV2$^{flox/flox}$;MerCreMer$^{+/-}$* myocytes were disturbed in the presence of RR at the same level as in TRPV2-deficient myocytes (Fig. 8f). Taken together, these findings suggest that TRPV2 activation is required for the formation of intercalated discs connecting neighbouring myocytes and their maturation into synchronously beating myocytes.

Stretch-dependent TRPV2 activation controls IGF-1 secretion. Substantial evidence from genetic mouse models has demonstrated the critical role of the IGF-1 receptor/PI3K/Akt pathway in maintaining physiological cardiac morphology and function[25]. Surprisingly, the connection with neighbouring myocytes and sarcomere orientation was maintained in TRPV2-deficient myocytes, when IGF-1 was added to cultures (Fig. 9a). Therefore, we measured IGF-1 secretion from cardiomyocytes in culture in response to cyclic stretch stimulation at 1 Hz for 30 min. IGF-1 secretion was markedly elevated in control

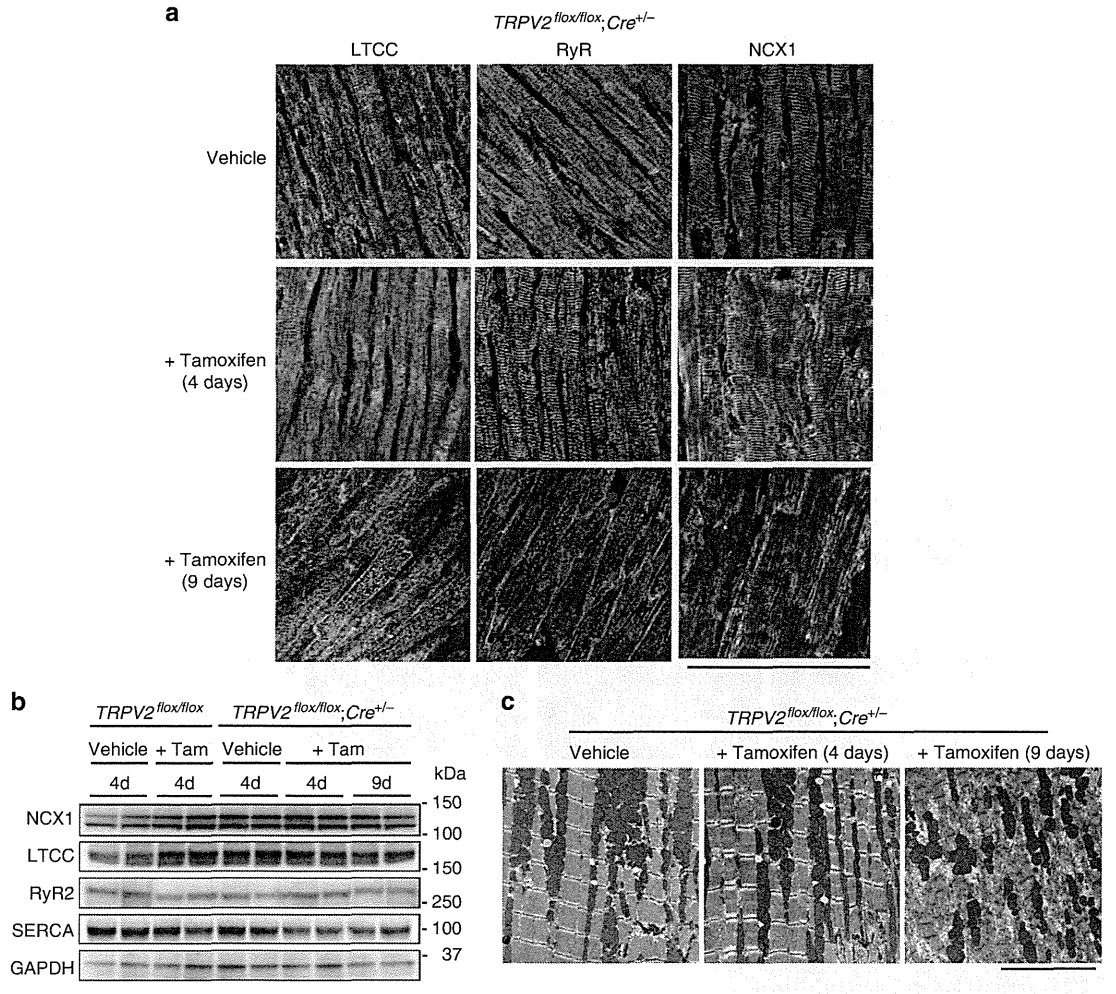

Figure 7 | Expression of Ca^{2+} handling protein by isolated cardiomyocytes and electron micrographs of myofibrils in TRPV2-deficient hearts. (**a**) Time-dependent changes in the localization of the Ca^{2+} regulatory proteins LTCC, RyR and NCX1 in tamoxifen-treated *TRPV2*$^{flox/flox}$;*Cre*$^{+/-}$ mice. Double staining with anti-LTCC antibody (green) and DAPI (blue) in cardiac muscle (left panels). Double staining with anti-RyR antibody (green) and DAPI (blue) in cardiac muscle (middle panels). Double staining with anti-NCX1 antibody (green) and DAPI (blue) in cardiomyocytes (right panels). Scale bar, 100 μm. (**b**) Expression of NCX1, LTCC, RyR and SERCA proteins in TRPV2-deficient heart extracts (10 μg per lane), using GAPDH as the internal control in cardiac muscle, (see full blots in Supplementary Fig. 6). (**c**) Electron micrographs of myofibrils in cardiomyocytes from *TRPV2*$^{flox/flox}$;*Cre*$^{+/-}$ mice, untreated or treated with tamoxifen. Scale bar, 5 μm.

myocytes and was blocked by the inhibitors of stretch-activated channels, Gd^{3+} or RR, whereas it was significantly reduced in TRPV2-deficient myocytes (Fig. 9b).

IGF-1 secreted from cardiomyocytes and fibroblast promotes the cardioprotective response to severe pressure overload by activating PI3K and its downstream effector Akt[26,27]. Patients with heart failure have been reported to have significantly lower IGF-1 levels compared with controls[28]. In *TRPV2*$^{flox/flox}$;*MerCreMer*$^{+/-}$ mice treated with tamoxifen for 3 or 4 days, *IGF-1*, *IGF-1 receptor*, *PI3Kα* and *Akt1* expression was significantly reduced (Fig. 9c–f). These observations suggest that the IGF-1 receptor/PI3K/Akt pathway is downregulated in TRPV2-deficient hearts.

Effects of IGF-1 administration in TRPV2-deficient hearts. To investigate whether the reduced IGF-1 signalling seen in TRPV2-deficient mice represented a significant molecular basis for their observed heart failure phenotype, we treated TRPV2-deficient mice with recombinant IGF-1. In normal mice, IGF-1 administration for 1 week resulted in an increase in cardiac mass and heart-to-body weight ratio (Fig. 9g,h). Remarkably, in TRPV2-deficient mice, administering IGF-1 prevented both the enlargement of the left ventricular diastolic dimensions and cardiac dysfunction (Fig. 9i,j). In addition, expression of *IGF-1 receptor*, *PI3Kα* and *Akt1* were all significantly increased by the administration of IGF-1 in TRPV2-deficient hearts (Supplementary Fig. 5). These results suggest that reduced IGF-1 signalling is a major factor in the heart failure observed in TRPV2-deficient mice. However, IGF-1 administration did not result in complete recovery, suggesting that other signalling pathways may also be impaired in TRPV2-deficient hearts.

Discussion

This study has shown a critical role for TRPV2 in the normal heart. TRPV2 is localized at intercalated discs, which are critical for detecting the mechanical forces generated by myocyte contraction. The elimination of TRPV2 from the mouse heart resulted in severe cardiac dysfunction within a few days (Fig. 3),

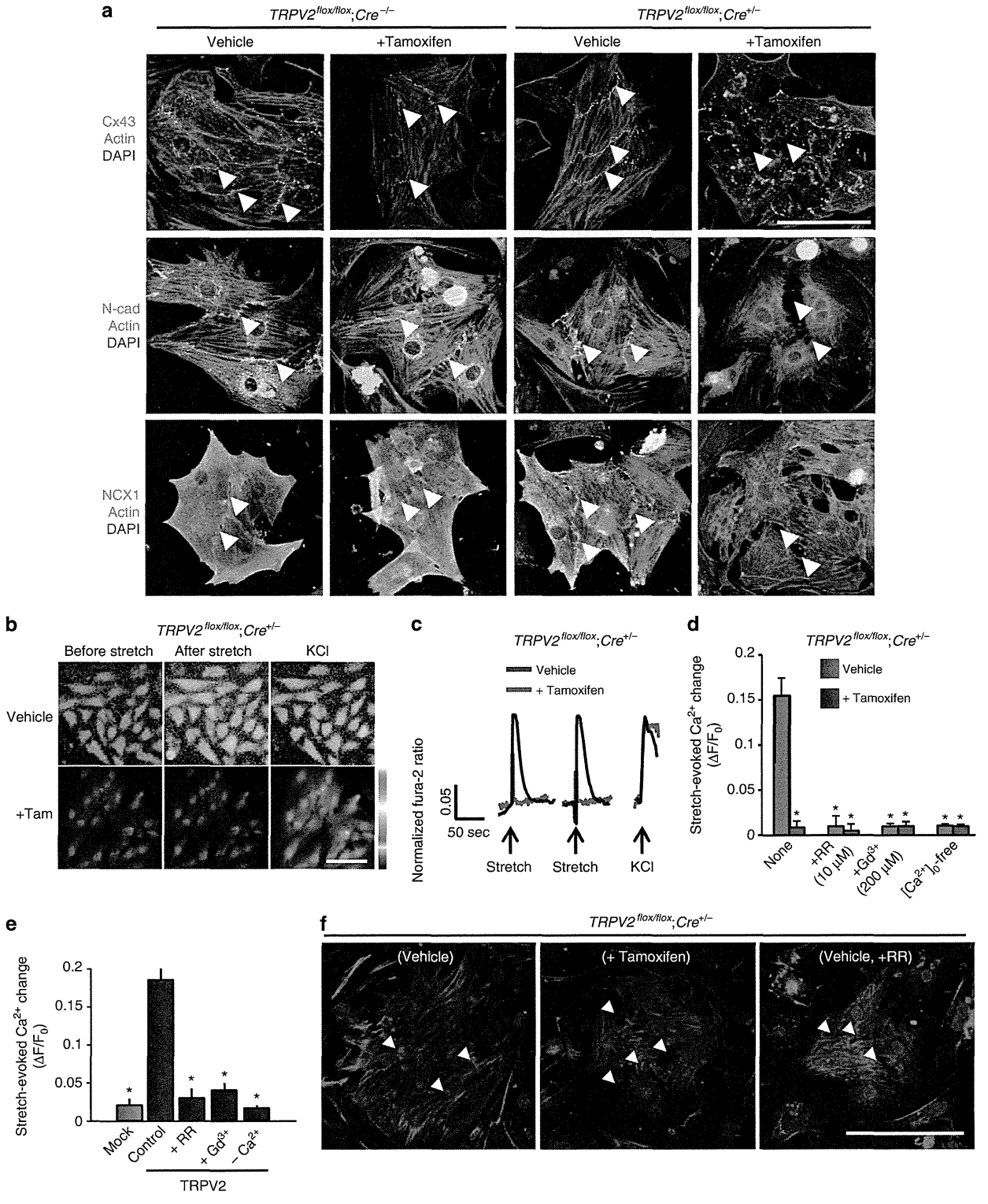

Figure 8 | Impairment of maturation into functional syncytia with synchronously beating cardiomyocytes in TRPV2-deficent newborn mice. (**a**) Isolated cardiomyocytes from *TRPV2*$^{flox/flox}$;*Cre*$^{-/-}$ or *TRPV2*$^{flox/flox}$;*Cre*$^{+/-}$ newborn mice. Triple staining with anti-connexin 43 antibody (green), phalloidin (red) and DAPI (blue) in cardiomyocytes (upper panels). Triple staining with anti-N-cadherin antibody (green), phalloidin (red) and DAPI (blue) in cardiomyocytes (middle panels). Triple staining with anti-NCX1 antibody (green), phalloidin (red) and DAPI (blue) in cardiomyocytes (lower panels). Scale bar, 100 μm. (**b**) Fura-2-imaging of stretch-induced intracellular Ca^{2+} dynamics in neonatal cardiomyocytes. Scale bar, 100 μm. (**c**) Representative trace of stretch-induced intracellular Ca^{2+} increase. (**d**) Effect of mechanosensitive channel inhibitors. Data are means ± s.e.m. *$P<0.01$ versus vehicle control ($n=19$–44). (**e**) Stretch-induced Ca^{2+} changes in ectopically expressed TRPV2 in HEK293 cells. Data are means ± s.e.m. *$P<0.01$ versus control. ($n=23$–37) (**f**) Isolated cardiomyocytes from newborn mice cultured with 10 μM rubidium red. Scale bar, 100 μm. Arrowheads, cell–cell junctions.

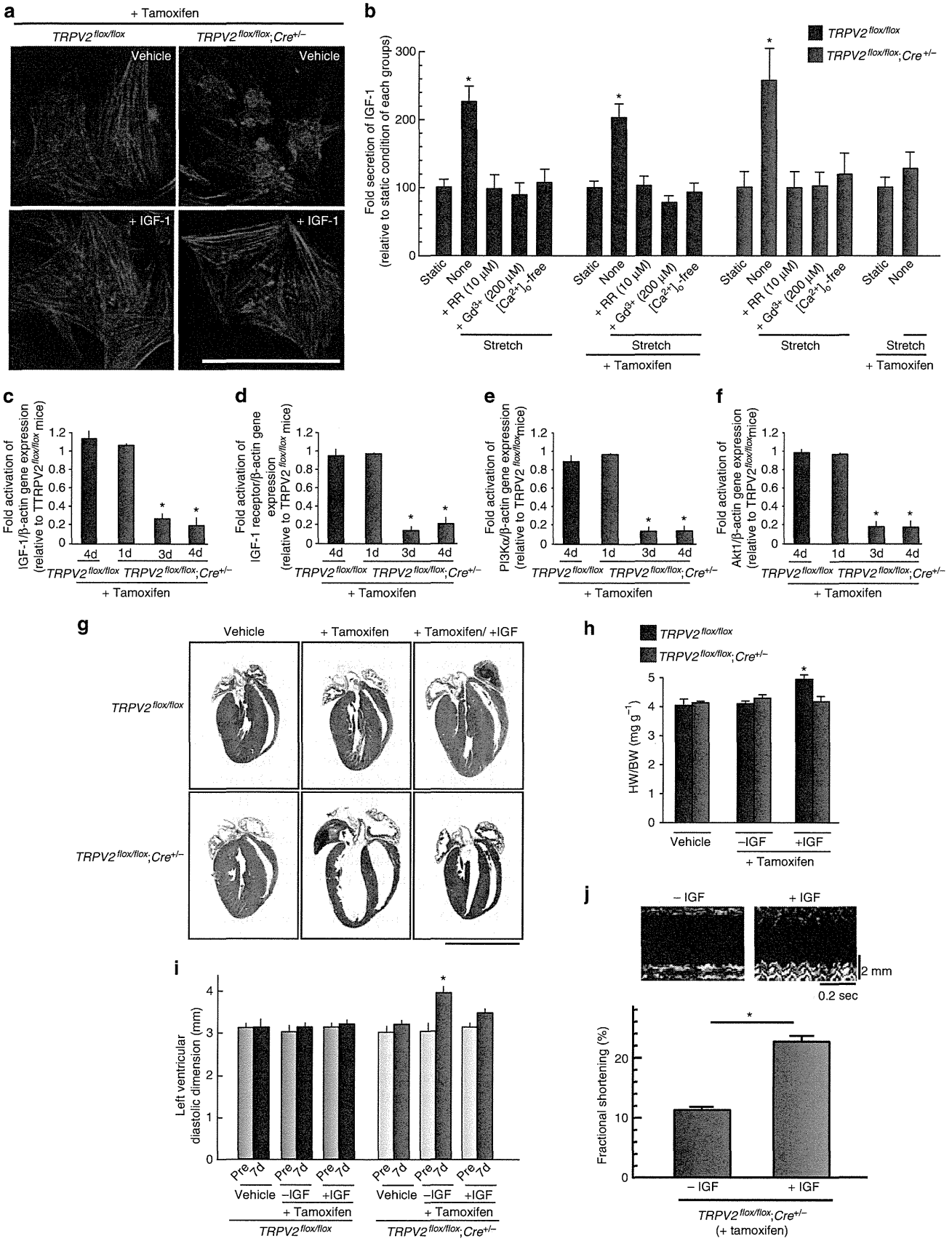

despite no impairment of myocyte contraction or E–C coupling efficiency (Fig. 6). These observations suggest that the functional integration with neighbouring cardiomyocytes was weakened in TRPV2-deficient hearts. It seems that cardiomyocytes sense inadequate functional output at a cellular level and respond by increasing the number of myofibrillar attachment sites in intercalated area[7]. In a failing heart, the elevated expression of adherens junction proteins and the increase in membrane convolution and interdigitation between neighbouring cardiomyocytes seems to lead to a decrease in the flexibility of the contractile tissue and increased stiffness[7]. In TRPV2-deficient hearts, the myofilaments were disassembled at their attachment sites to intercalated discs (Fig. 4a). The TRPV2-deficient myocytes did not seem to sense the inadequate functional output or the severe cardiac dysfunction and therefore might have difficulty maintaining the integrity of their intercalated discs. On the other hand, cultured neonatal cardiomyocytes from TRPV2-deficient mice showed impaired formation of intercalated discs and translocation of connexin 43 and N-cadherin into cell–cell adhesion sites, and no spontaneous, synchronized beating (Fig. 8a). The TRPV2 inhibitor, RR, also affected intercalated disc formation in neonatal cardiomyocytes (Fig. 8f), implicating TRPV2 activity in the maintenance of intercalated disc integrity as well as their formation. Further experiments are needed to elucidate the molecular mechanism involved in maintaining intercalated disc structure and exactly how this function depends upon TRPV2.

It is possible that TRPV2 has a pivotal role as an anchoring protein for myofibrils at intercalated discs, coordinating the transmission of mechanical forces regardless of its channel activity. The transmission of the force generated by contracting myofibrils is mediated by so-called adherens junctions, which are composed of transmembrane proteins of the cadherin family and which, in the cytoplasm, are coupled to the contracting sarcomeres by members of the catenin family[7]. Reportedly, TRPV4 associates with adherens junctions via α-catenin in the human bladder urothelium[29]. In common with several members of other TRP subfamilies[30], the cytoplasmic region of TRPV2 is likely to couple to a rigid intracellular structural network and form 'mechanosensitive Ca^{2+}-signalosomes' at intercalated discs. If so, eliminating TRPV2 is therefore likely to interrupt mechanical coupling with neighbouring myocytes at intercalated discs, causing severe cardiac dysfunction.

In addition, we showed a significant reduction of stretch-dependent IGF-1 secretion in TRPV2-deficient myocytes (Fig. 9b), and a downregulation of IGF-1 receptor/PI3K/Akt signalling in TRPV2-deficient hearts (Fig. 9c–f). IGF-1 is continuously secreted in the normal state and in response to mechanical stress dependent on the intracellular Ca^{2+} concentration[25,26,31]; this in turn modulates myocyte PI3K signalling, which is involved in myocardial hypertrophy and heart failure[25]. It appears that the TRPV2 activation-dependent IGF-1 secretion of cardiomyocytes controls the equilibrium balance of intracellular IGF-1 receptor/PI3K/Akt signalling in response to haemodynamic stress. This forms a molecular basis for the myocyte mechanical feedback mechanism in the normal state and in response to haemodynamic stress, which is required to maintain cardiac structure and function. Therefore, loss of TRPV2 not only leads to a rapid and severe decline in normal cardiac pump function, but also triggers subsequent cellular dysfunction in individual myocytes.

TRP channels are unique cellular sensors responding to a wide variety of extracellular and intracellular signals, including mechanical and osmotic stress[32]. The present study shows that TRPV2 is a candidate molecule for stretch-activated channels in myocyte intercalated discs, and is crucial for the mechanical stimulation-dependent Ca^{2+} signalling of cardiomyocytes. However, it is unclear whether TRPV2 channels directly transduce mechanical stimuli or are part of a downstream signalling pathway, as discussed below. Several regulatory interactions between TRPV2 cytoplasmic domains and various signalling molecules have been investigated. Mercado *et al.*[33] proposed that PIP_2 is constitutively associated with the C-terminal domain of TRPV2, promoting its inhibition Ca^{2+}-dependently. It is not yet certain that TRPV2 directly senses membrane lipid stretching through PIP_2 breakdown and diacylglycerol production, as has been shown for other mechano-sensitive channels[34,35]. Therefore, to clarify the regulatory mechanism of TRPV2 activation, further electrophysiological investigations will be needed in the future.

TRPV2 has been reported to translocate from an intracellular compartment to the plasma membrane in response to IGF-1 and intracellular Ca^{2+} concentration[17,36]. Therefore, the appropriate control of these mediators might be needed for the localization of TRPV2 to the membrane in intercalated discs in working hearts. It is possible that the transmission and generation of mechanical force during contraction in response to haemodynamic stress provides the control for IGF-1 production and intracellular Ca^{2+} concentrations, in which TRPV2 plays a pivotal role by continuously monitoring mechanical stress. TRPV2 activity is also directly controlled by PI3K activity, and this is independent of channel translocation to the plasma membrane[37]. Activation of PI3K by growth factors results in PIP_3 synthesis, by the phosphorylation of PIP_2 (ref. 25). Thus, TRPV2 activity is also likely to be regulated by the PIP_2 content, dependent on PI3K activity, and interactions with other lipids in intercalated discs. However, little is known about the lipid composition of intercalated discs. Taken together, these findings suggest that the lipid composition and potentiation of the IGF-1 receptor/PI3K/Akt signalling cascade in response to haemodynamic stress are key factors for TRPV2 activation at intercalated discs in the heart.

This study has identified a molecular basis for the maintenance of cardiac structure and function, through myocyte mechanical feedback systems, in which TRPV2 plays a pivotal role (Fig. 10). The integrity of intercalated discs has a large impact on force transmission and generation during muscle contraction, and is reflected in the effect of mechanical feedback on the quality of myocytes in the heart. Eliminating TRPV2 had no effect on Ca^{2+} handling in myocyte E–C coupling (Fig. 6b–f), which is generated at dyads formed between a T-tubule and the junctional part of the sarcoplasmic reticulum. It appears that the Ca^{2+} signalling

Figure 9 | Impairment of stretch-dependent IGF-1 secretion and IGF-1 receptor/PI3K/Akt pathway in TRPV2-deficient yocytes. (**a**) Isolated cardiomyocytes from newborn mice cultured with 10 μM IGF-1. Scale bar, 100 μm. (**b**) Stretch-dependent IGF-1 secretion by cardiomyocytes. $^*P<0.05$ versus the other groups. Data are means ± s.e.m. (**c–f**) *IGF-1, IGF-1 receptor, PI3Kα and Akt* expression level in TRPV2-deficient hearts ($n=3$ mice per group). $^*P<0.05$ versus non-treated $TRPV2^{flox/flox}$ mice. Data are means ± s.e.m. (**g**) Histological analysis 7 days after onset of IGF-1 administration and tamoxifen treatment in TRPV2-deficient mice. Scale bar, 5 mm. (**h**) HW/BW ratio. Data are means ± s.e.m. ($n=5$–12 per group) $^*P<0.05$ for tamoxifen-treated $TRPV2^{flox/flox};Cre^{+/-}$ mice versus IGF-1-treated $TRPV2^{flox/flox};Cre^{+/-}$ mice after 7 days. (**i,j**) Echocardiographic parameters ($n=3$ per group). (**i**) Data are means ± s.e.m. $^*P<0.05$ versus all the other groups. by two-way analysis of variance with Bonferroni's *post hoc* test.

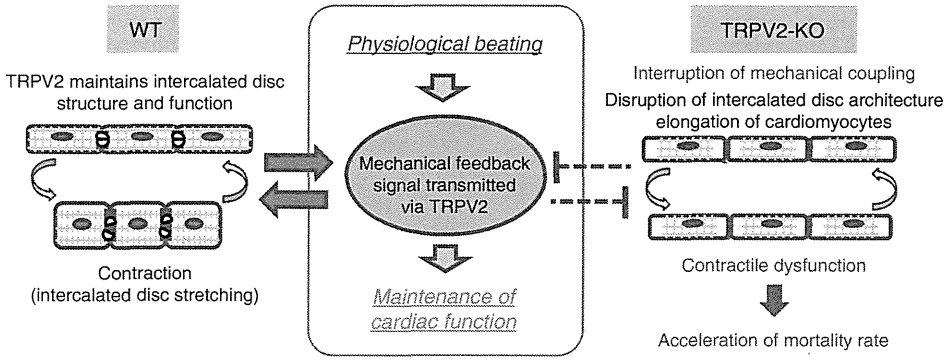

Figure 10 | Role of TRPV2 within the working heart. In wild-type mice, TRPV2 protein (yellow) is located in the intercalated discs (red), which is cyclically stretched and accompanied by cardiac contractions within the working heart. The mechanical feedback signal transmitted via TRPV2 is crucial for the maintenance of cardiomyocytes. TRPV2 ablation leads to the disruption of the intercalated disc architecture (red), and disorganization of sarcomere myofibril proteins at the intercalated discs (orange). These TRPV2-KO myocytes show contractile dysfunction. Therefore, the mortality rate of TRPV2-KO mice is accelerated. Thus, the mechanical feedback signal within the working heart integrates myocyte structure and function, with TRPV2 playing a pivotal role.

involved in myocyte E–C coupling and the mechanical signal mediated by TRPV2 are spatially and temporally controlled by different signals in cardiomyocytes. Further studies might clarify the molecular mechanism of mechanotransduction mediated by TRPV2 in cardiomyocytes, and so improve our understanding of cardiac development and maturation, hypertrophic remodelling in the heart and the pathophysiology of heart disease.

Recently, Rubinstein *et al.*[38] reported the cardiac function of TRPV2-KO mice expressing *Cre* under the control of the cytomegalovirus promoter generated by Park *et al*[39]. They observed that cardiac function declined in TRPV2-deficient mice compared with controls, despite no histological abnormality[38]. Although there are differences in the severity of cardiac dysfunction and the depression of myocyte contractility, these results are consistent with our observations. However, the construction of their TRPV2-KO mice differed from our model in the site at which the partial elimination occurred, which corresponded to the channel pore and carboxy-terminal region of TRPV2, using a ubiquitous promoter, and the genetic background of the mice (B6129SF2/J)[39]. Park *et al.*[39] have reported that their model was susceptible to perinatal lethality but displayed normal thermal and mechanical nociception. They therefore suggested the possibility that compensatory mechanisms prevented the obvious phenotype of TRPV2-deficient cells being reflected in their KO mice[39]. On the other hand, the cardiac-specific elimination of TRPV2 in this study affected neither the embryonic development nor the growth after birth, in the absence of tamoxifen administration. Taken together, we believe that the acute elimination of TRPV2 function in our model might circumvent any hypothetical compensatory process.

Methods

Animals. Mice were housed under a 12-h light–dark cycle in a temperature-controlled environment. All the experiments were performed in male mice aged 10 weeks old (weighing 22–24 g). Littermates were used in this study to randomize genetic variation. All animal experiments were approved by the Animal Research Committee of Okayama University (Okayama, Japan), and were performed in accordance with institutional guidelines.

Generation of TRPV2 conditional KO mice. All experiments requiring gene recombination in this study were carried out in accordance with the institutional guideline of Okayama University (Okayama, Japan). Using cloned TRPV2 cDNA (accession code. NM011706) as a probe, we screened a genomic library constructed from C57/BL6J mouse DNA. The genomic clone was used to generate the targeting vector shown in Supplementary Fig. 1, which was linearized for electroporation into C57/BL6J ES cells. After selection, G418-resistant ES clones were screened for the presence of the targeted locus by southern blot analysis. Targeted ES cells were microinjected into Balb/c mouse blastocysts, and germline transmission of the TRPV2 conditional null alleles was confirmed by southern blotting and PCR genotyping using genomic DNA extracted from mouse tail veins. We crossed mice carrying a $TRPV2^{flox}$ allele with transgenic mice (*MerCreMer*) expressing tamoxifen-inducible cardiomyocyte-specific Cre recombinase to produce $TRPV2^{flox/flox}$;$MerCreMer^{+/-}$ mice. Germline transmission of TRPV2 conditional null alleles was confirmed by southern blotting and PCR genotyping using the primer pair 5′-TTAAATGACTTGTGAGGGAGATAGC-3′ and 5′-CAAGTAACA CAATCTACCCAAGGTC-3′, yielding 322 (wild-type) and 369 (null allele) bp products. To induce *Cre*-mediated recombination, we injected 10-week-old male $TRPV2^{flox/flox}$;$MerCreMer^{+/-}$, $TRPV2^{flox/+}$;$MerCreMer^{+/-}$ and $TRPV2^{flox/flox}$;$MerCreMer^{-/-}$ mice intraperitoneally with 8 mg kg^{-1} tamoxifen (Sigma) once daily for 4 consecutive days. Tamoxifen injection and subsequent analyses were performed in a blinded fashion.

Electrocardiography. Transthoracic electrocardiography (ECG) was used to evaluate cardiac function with the Aplio 300 (Toshiba Medical System) and a 14-MHz transducer. The 10-week-old male mice were anesthetized initially with 2% isoflurane, and then at 1% during the examination. Left ventricular short-axis dimensions at the tip of the papillary muscles were measured on M-mode. Fractional shortening was calculated as (LVDd–LVDs)/LVDd × 100 (%).

Blood pressure measurement. Chronic measurements of blood pressure and ECG were performed on unrestrained, conscious mice (10-week-old, male) using a commercially available telemetry and computer-based data acquisition system (Data Sciences International) according to the manufacturer's instructions. Briefly, a pressure-sensing catheter was implanted in the thoracic aorta via the left carotid artery, and two electrodes were placed subcutaneously on the right shoulder and left inguinal region to record lead II ECG under anaesthesia with 2% isoflurane inhalation. Mice were returned to their home cage (placed on top of telemetry receivers), and blood pressure and ECG were continuously monitored and recorded.

Administration of IGF-1. Recombinant human IGF-I was purchased from Cell Science, and diluted with 0.9% NaCl at a concentration of 10 mg ml^{-1} and administered to mice (60 μg per day) by continuous infusion (0.25 μl h^{-1}) using a mini osmotic pump (Alzert 1002). IGF-1 administration and tamoxifen treatment were started at the same time. Control mice received vehicle alone.

Neonatal cardiomyocyte culture. Primary cardiomyocyte cultures were prepared from ventricles of 1-day-old mice by very gentle trypsinization at room temperature, by a modification of preparation methods from rat neonatal heats[40]. Hearts were rapidly removed from neonatal $TRPV2^{flox/flox}$;$MerCreMer^{+/-}$ or $TRPV2^{flox/flox}$;$MerCreMer^{-/-}$ mice anesthetized with an overdose of diethyl ether. The ventricles were excised, cut into several pieces and washed three times with 10 ml ice-cold phosphate-buffered saline for 1 min by gentle shaking. The tissue pieces were digested three times with 0.06% trypsin in DMEM (8 ml) for 8 min at 37 °C by gentle agitation. The cell suspension was resuspended in DMEM with 10% fetal calf

serum (FCS) to stop trypsinization, and was centrifuged at 14*g* for 3 min. The cell pellets were resuspended in fresh DMEM containing 10% FCS, and plated on collagen-coated 24-well dishes at a density of 4×10^4 cells per well and maintained in DMEM containing 10% FCS. The formation of myocytes clusters and the spontaneous synchronized beating were confirmed by inverted microscope (CKX41, Olympus).

Stretch stimulation of cardiomyocytes. For stretch stimulation of cardiomyocytes, the cell suspension were plated on 1 cm^2 collagen-coated polydimethylsiloxane stretch chambers at 2×10^5 cells per well, and cultured. After 24 h, primary cardiomyocytes were divided into two groups and maintained for up to 2 days in DMEM containing 10% FCS, with or without tamoxifen (0.2 $\mu M\,ml^{-1}$). Membranes were uniformly stretched by 20% for 3 s, using a computer-controlled stepping motor machine (STB-150, STREX), by a slight modification of cell-stretch culture methods[41]. One end of the chamber was firmly attached to a fixed frame, while the other was attached to a movable frame connected to a motor-driven shaft. The amplitude and frequency of stretch were controlled by a programmable microcomputer. The silicon membrane was uniformly stretched over the whole membrane area, and the lateral thinning did not exceed 1% at 20% stretch. TRPV2 deficiency did not have a discernible impact on the cardiomyocytes' ability to adhere to the membrane, although the cell–cell interfaces with neighbouring myocytes were expanded.

Stretch-induced Ca^{2+}-transients in newborn cardiomyocytes. Stretch-induced Ca^{2+} transients were examined in cardiomyocytes loaded with 2 μM fura-2 acetoxymethyl ester (fura-2) for 30 min at 37 °C and maintained in standard Tyrode's solution under continuous flow using a microperfusion system. Fura-2-loaded cells were alternately excited at 340 and 380 nm using a Lambda DG-4 Ultra High Speed Wavelength Switcher (Sutter Instruments) coupled to an inverted IX71 microscope with a UApo 20 × /0.75 objective lens (Olympus). Fura-2 fluorescent signals were recorded (ORCA-Flash 2.8; Hamamatsu Photonics) and analysed by a ratiometric fluorescence method using MetaFluor software (version 7.7.5.0; Molecular Devices).

Isolation of adult mouse ventricular myocytes. Ventricular myocytes were obtained from 10-week-old male *TRPV2$^{flox/flox}$;MerCreMer$^{+/-}$* and *TRPV2$^{flox/flox}$;MerCreMer$^{-/-}$* mice by a slight modification of Shioya's methods[42]. Hearts were rapidly removed from adult *TRPV2$^{flox/flox}$;MerCreMer$^{+/-}$* or *TRPV2$^{flox/flox}$;MerCreMer$^{-/-}$* mice anesthetized with an overdose of pentobarbital (300 $mg\,kg^{-1}$, intraperitoneally), and Langendorff perfused at a constant hydrostatic pressure of 70 cm H_2O at 37 °C using cell isolation buffer (CIB) supplemented with 0.4 mM EGTA (EGTA–CIB), which chelates calcium within the heart. CIB contained 130 mM NaCl, 5.4 mM KCl, 0.5 mM $MgCl_2$, 0.33 mM NaH_2PO_4, 22 mM glucose, 50 $nM\,ml^{-1}$ bovine insulin (Sigma) and 25 HEPES-NaOH (pH = 7.4). Insulin was used from 1 $U\,ml^{-1}$ stock solution in 0.1 mM HCl (pH = 4.0). EGTA was from 400 mM stock in 1 M NaOH (pH = 7.8). The perfusate was then switched to the enzyme solution (15 ml), which was CIB supplemented with 0.3 mM $CaCl_2$, 1 $mg\,ml^{-1}$ collagenase (Worthington Biochemical), 0.06 $mg\,ml^{-1}$ trypsin (Sigma) and 0.06 $mg\,ml^{-1}$ protease (Sigma). Once the tissue had undergone complete digestion, the ventricles were excised, cut into several pieces and further digested in fresh enzyme solution (15 ml) for 15–20 min at 37 °C until they were mostly dissociated. In this enzyme solution, the $CaCl_2$ level was increased to 0.7 mM, and 2 $mg\,ml^{-1}$ BSA (Sigma) was supplemented. The cell suspension was centrifuged at 14*g* for 3 min. The cell pellet (~0.1 ml) was resuspended in CIB supplemented with 1.2 mM $CaCl_2$ and 2 $mg\,ml^{-1}$ BSA, and then incubated at 37 °C for 10 min, centrifuged (14*g*, 3 min) and resuspended in 10 ml Tyroad solution supplemented with 2 $mg\,ml^{-1}$ BSA. Tyrode's solution contained 140 mM NaCl, 5.4 mM KCl, 1.8 mM $CaCl_2$, 0.5 mM $MgCl_2$, 0.33 mM NaH_2PO_4, 11 mM glucose and 5 mM HEPES-NaOH (pH = 7.4)[40,42].

Cell shortening and Ca^{2+} transients in adult cardiomyocytes. Isolated cardiomyocytes were loaded with 10 $\mu mol\,l^{-1}$ Indo-1 AM (Invitrogen) and electrically stimulated at 1 Hz using a two-platinum electrode insert connected to a bipolar stimulator (Nihon Kohden, SEN-3301) on the stage of an inverted microscope (IX71, Olympus) with a × 20 water immersion objective lens (UApo N340, Olympus). Calcium transients were measured as the ratio of fluorescence emitted at 405/480 nm after excitation at 340 nm using a high-performance Evolve EMCCD camera (Photometrics). Cardiomyocytes were maintained under continuous flow in standard Tyrode's solution, exchanged using a microperfusion system. For measuring caffeine-induced calcium transients, cells were paced at 1 Hz prior to induction of caffeine contractures. Electrical stimulation was stopped 15 s before rapid perfusion with a 10 $mmol\,l^{-1}$ caffeine solution. The experiments were recorded and analysed using MetaMorph software (version 7.7.1.0; Molecular Devices). Results were the means of the fluorescent signals from 10–20 cardiomyocytes from a single heart.

Measure of IGF-1 concentration. IGF-1 concentrations were measured in conditioned media from stretched and unstretched myocytes in a sandwich ELISA using mouse standards, according to the manufacturer's guidelines (R&D Systems), which quotes the sensitivity of this assay as 30 $ng\,ml^{-1}$. Standard curves and positive controls were included in each assay, and IGF-1 concentrations were obtained by interpolation.

Real-time PCR. The Mouse PI3K-AKT Signalling Pathway RT^2 Profiler PCR Array was purchased from Qiagen. Total RNA extracted from *TRPV2$^{flox/flox}$;MerCreMer$^{+/-}$* or *TRPV2$^{flox/flox}$;MerCreMer$^{-/-}$* hearts with or without tamoxifen were reverse transcribed into cDNA with oligo (dT) primers using Superpscript III. Real-time PCR was performed with Step-One plus^{TM} (Applied Biosystem). Statistical analysis of the results was performed with the $^{\Delta}Ct$ value ($Ct_{\text{gene of interest}} - Ct_{\beta\text{-actin}}$). Relative gene expression was obtained using the $^{\Delta\Delta}Ct$ method ($Ct_{\text{sample}} - Ct_{\text{calibrator}}$) using the *TRPV2$^{flox/flox}$;MerCreMer$^{-/-}$* hearts without tamoxifen as a calibrator.

Histology. Hearts were excised and immediately fixed in buffered 4% paraformaldehyde, embedded in paraffin and sectioned to a thickness of 4 μm. We stained serial sections of samples with Masson's trichrome to evaluate gross morphology and fibrosis. The preparations were examined under a light microscope (SZX7 or BX43, Olympus).

Electron microscopy. For electron microscopy, excised hearts were fixed in 2% paraformaldehyde/2% glutaraldehyde in 0.1 M phosphate buffer, postfixed with 2% OsO4 in 0.1 M phosphate buffer and stained with uranyl acetate and lead citrate. The microtome sections were examined under a JEM-1200 electron microscope (Nihondensi Co., Japan).

Antibodies. The following antibodies were used for immunostaining or immunoblot analysis: anti-TRPV2 (1:200 dilution, AB5398, Millipore); anti-vinculin (1:100 dilution, V9131, Sigma); anti-connexin 43 (1:100 dilution, C6219, Sigma); anti-N-cadherin (1:100 dilution, 3B9, life technologies); anti-Cav3 (1:1,000 dilution, 610420, BD Pharmingen,); anti-LTCC (1:1,000 dilution, ACC033, Alomone); anti-SERCA (1:1,000 dilution, MA3919, Thermo); and anti-RyR (1:1,000 dilution, MA3916, Thermo). The anti-NCX antibody was generated in our laboratory (1:1,000 dilution).

Immunocytochemistry. For immunocytochemistry, 5 μm frozen heart sections embedded in OCT compound (Tissue-Tek) were permeabilized with 0.1% Triton X-100 and incubated with primary antibodies. For immunostaining of rat cardiomyocytes, cells immobilized on collagen-coated glass slides were fixed with 4% paraformaldehyde for 15 min at room temperature, permeabilized with 0.1% Triton X-100 and then stained with primary antibodies.These samples were then treated with Alexa Flour 488-conjugated anti-rabbit IgG (A11008, Life Technologies) or Alexa Flour 488-conjugated anti-mouse IgG (A11001, Life Technologies). Cells or secrions were examined using a confocal microscope (Fluoview FV1000, Olympus) mounted on an Olympus IX81 epifluorescence microscope with a UPlanSApo × 60/1.35 oil immersion objective lens (Olympus).

Immunoblotting. Mice hearts and kidneys were homogenized in a Hiscotron homogenizer (NITI-ON) in lysis buffer containing 20 mM HEPES (pH 7.4), 150 mM NaCl, 1% sodium deoxycholate, 1% SDS, 2 $\mu g\,ml^{-1}$ leupeptin, 1 $\mu g\,ml^{-1}$ aprotinin, 200 μM phenylmethylsulfonyl fluoride, and 200 μM benzamidine hydrochloride. The lysates were centrifuged at 100,000*g* for 20 min and the supernatants were used for immunoblot analysis. Immunoreactive bands were visualized using a chemiluminescence detection system (Perkin Elmer) and an LAS3000 Luminescent Image Analyzer (Fuji Film).

Data analysis. Data were analysed by individuals who were blinded to the genotype, drug treatment or operation. Data presented here were reproducible in at least three independent experiments. Results are shown as the mean ± s.e.m. Paired data were evaluated using a Student's *t*-test. Two-way analysis of variance with Bonferroni's *post hoc* test was used for multiple comparisons wherever appropriate. The Kaplan–Meier method with a log-rank test was used for survival analysis. $P < 0.05$ was considered statistically significant.

References

1. Engler, A. J., Sen, S., Sweeney, H. L. & Discher, D. E. Matrix elasticity directs stem cell lineage specification. *Cell* **126,** 677–689 (2006).
2. McCain, M. L. & Parker, K. K. Mechanotransduction: the role of mechanical stress, myocyte shape, and cytoskeletal architecture on cardiac function. *Eur. J. Physiol.* **462,** 89–104 (2011).
3. Hill, J. A. & Olson, E. N. Cardiac plasticity. *New Engl. J. Med.* **358,** 1370–1380 (2008).
4. Estigoy, C. B. *et al.* Intercalated discs: multiple proteins perform multiple functions in non-failing and failing human hearts. *Biophys. Rev.* **1,** 43–49 (2009).
5. Noorman, M. *et al.* Cardiac cell-cell junctions in health and disease: electrical versus mechanical coupling. *J. Mol. Cell. Cardiol.* **47,** 23–31 (2009).

6. McCain, M. L. *et al.* Cooperative coupling of cell-matrix and cell-cell adhesions in cardiac muscle. *Proc. Natl Acad. Sci. USA* **109,** 9881–9886 (2012).
7. Perriard, J.-C., Hirschy, A. & Ehler, E. Dilated cardiomyopathy: a disease of the intercalated disc? *Trends Cardiovasc. Med.* **13,** 30–35 (2003).
8. Kostetskii, I. *et al.* Induced deletion of the N-cadherin gene in the heart leads to dissolution of the intercalated disc structure. *Circ. Res.* **96,** 346–354 (2005).
9. Parlakian, A. *et al.* Temporally controlled onset of dilated cardiomyopathy through disruption of the SRF gene in adult heart. *Circulation* **112,** 2930–2939 (2005).
10. Li, J. *et al.* Loss of alphaT-catenin alters the hybrid adhering junctions in the heart and leads to dilated cardiomyopathy and ventricular arrhythmia following acute ischemia. *J. Cell Sci.* **125,** 1058–1067 (2012).
11. Wang, X. & Gerdes, A. M. Chronic pressure-overload cardiac hypertrophy and failure in guinea pigs: III. Intercalated disc remodeling. *J. Mol. Cell. Cardiol.* **31,** 333–343 (1999).
12. Alcalai, R., Metzger, S., Rosenheck, S., Meiner, V. & Chajek-Shaul, T. A recessive mutation in desmoplakin causes arrhythmogenic right ventricular dysplasia, skin disorder, and woolly hair. *J. Am. Coll. Cardiol.* **42,** 319–327 (2003).
13. Protonotarios, N. & Tsatsopoulou, A. Naxos disease and Carvajal syndrome: cardiocutaneous disorders that highlight the pathogenesis and broaden the spectrum of arrhythmogenic right ventricular cardiomyopathy. *Cardiovasc. Pathol.* **13,** 185–194 (2004).
14. Basso, C. *et al.* Ultrastructural evidence of intercalated disc remodeling in arrhythmogenic right ventricular cardiomyopathy: an electron microscopy investigation on endomyocardial biopsies. *Eur. Heart. J.* **27,** 1847–1854 (2006).
15. Balse, E. *et al.* Dynamic of ion channel expression at the plasma membrane of cardiomyocytes. *Physiol. Rev.* **92,** 1317–1358 (2012).
16. Sharif-Naeini, A. *et al.* TRP channels and mechanosensory transduction: insights into the arterial myogenic response. *Eur. J. Physiol.* **456,** 529–540 (2008).
17. Iwata, Y. *et al.* A novel mechanism of myocyte degeneration involving the Ca^{2+}-permeable growth factor-regulated channel. *J. Cell Biol.* **161,** 957–967 (2003).
18. Muraki, K. *et al.* TRPV2 is a component of osmotically sensitive cation channels in murine aortic myocytes. *Cir. Res.* **93,** 829–838 (2003).
19. Sohal, D. S. *et al.* Temporally regulated and tissue-specific gene manipulations in the adult and embryonic heart using a tamoxifen-inducible Cre protein. *Cir. Res.* **89,** 20–25 (2001).
20. Hall, M. E., Smith, G., Hall, J. E. & Stec, D. E. Systolic dysfunction in cardiac-specific ligand-inducible MerCreMer transgenic mice. *Am. J. Physiol. Heart Cir. Physiol.* **301,** H253–H260 (2011).
21. Bito, V., Heinzel, F. R., Biesmans, L., Antoons, G. & Sipid, K. R. Crosstalk between L-type Ca^{2+} channels and sarcoplasmic reticulum: alterations during cardiac remodeling. *Cardiovasc. Res.* **77,** 315–324 (2008).
22. Verdonck, F., Mubagwa, K. & Sipid, K. R. [Na^+] in the subsarcolemmal 'fuzzy' space and modulation of $[Ca^{2+}]_i$ and contraction in cardiac myocytes. *Cell Calcium* **35,** 603–612 (2004).
23. Atherton, B. T., Meyer, D. M. & Simpson, D. G. Assembly and remodelling of myofibrils and intercalated discs in cultured neonatal rat heart cells. *J. Cell. Sci.* **86,** 233–248 (1986).
24. Bridget, T. J., Yipi, S., Philip, A. G., Fredrick, S. & Timothy, M. G. Ca^{2+} influx through mechanosensitive Ca^{2+} channels inhibits neurite outgrowth in opposition to other influx pathways and release from intracellular stores. *J. Neurosci.* **26,** 5656–5664 (2006).
25. Bianca, C. B., Kate, L. W., Lynette, P. & Julie, R. M. Molecular distinction between physiological and pathological cardiac hypertrophy: experimental findings and therapeutic strategies. *Phamacol. Therapeutics* **128,** 191–227 (2010).
26. Takeda, N. *et al.* Cardiac fibroblasts are essential for the adaptive response of the murine heart to pressure overload. *J. Clin. Invest.* **120,** 254–265 (2010).
27. Guo, D. *et al.* Loss of PI3Kγ enhances cAMP-dependent MMP remodeling of the myocardial N-cadherin adhesion complexes and extracellular matrix in response to early biomechanical stress novelty and significance. *Cir. Res.* **107,** 1275–1289 (2010).
28. Kontoleon, P. E. *et al.* Hormonal profile in patients with congestive heart failure. *Int. J. Cardiol.* **87,** 179–183 (2003).
29. Janssen, D. A. W. *et al.* The mechanoreceptor TRPV4 is localized in adherens junctions of the human bladder urothelium: a morphological study. *J. Urol.* **186,** 1121–1127 (2011).
30. Montell, C. TRP channels in *Drosophila* photoreceptor cells. *J. Physiol.* **567,** 45–51 (2005).
31. Cao, P., Maximov, A. & Sudhof, T. C. Activity-dependent IGF-1 exocytosis is controlled by the Ca^{2+}-sensor synaptotagmin-10. *Cell* **145,** 300–311 (2011).
32. Christensen, A. P. & Corey, D. P. TRP channels in mechanotransduction: direct or indirect activation? *Nat. Rev. Neurosci.* **8,** 510–521 (2007).
33. Mercado, J., Gordon-Shaag, A., Zagotta, W. N. & Gordon, S. E. Ca^{2+}-dependent desensitization of TRPV2 channels is mediated by hydrolysis of phosphatidylinositol 4,5-phosphate. *J. Neurosci.* **30,** 13338–13347 (2010).
34. Spassova, M. A., Hewavitharana, T., Xu, W., Soboloff, J. & Gill, D. L. A common mechanism underlies stretch activation and receptor activation of TRPC6 channels. *Proc. Natl Acad. Sci. USA* **103,** 16586–16591 (2006).
35. Chemin, J. *et al.* A phospholipid sensor controls mechanogating of the K+ channel TREK-1. *EMBO J.* **24,** 44–53 (2005).
36. Kanzaki, M. *et al.* Translocation of a calcium-permeable cation channel induced by insulin-like growth factor-I. *Nat. Cell Biol.* **1,** 165–170 (1999).
37. Penna, A. *et al.* PI3-kinase promotes TRPV2 activity independently of channel translocation to plasma membrane. *Cell Calcium* **39,** 495–507 (2006).
38. Rubinstein, J. *et al.* Novel role of transient receptor potential vanilloid 2 in the regulation of cardiac performance. *Am. J. Physiol. Heart Circ. Physiol.* **306,** H574–H584 (2014).
39. Park, U. *et al.* TRP vanilloid 2 knock-out mice are susceptible to perinatal lethality but display normal thermal and mechanical nociception. *J. Neurosci.* **31,** 11425–11436 (2011).
40. Katanosaka, Y. *et al.* Calcineurin inhibits Na^+/Ca^{2+} exchange in phenylephrine-treated hypertrophic cardiomyocytes. *J. Biol. Chem.* **280,** 5764–5772 (2005).
41. Katanosaka, Y. *et al.* Analysis of cyclic stretch responses using cell-adhesion-patterned cells. *J. Biotechnol.* **133,** 82–89 (2008).
42. Shioya, T. A simple technique for isolating healthy heart cells from mouse models. *J. Physiol. Sci.* **57,** 327–335 (2007).

Acknowledgements

This work was supported by Grants-in-Aid from the Ministry of Education, Culture, Sports, Science, and Technology of Japan (grant numbers 21300166 to Y.K. and 22240056 to K.N.), by the Japan Society for the Promotion of Science through the "Funding program for Next Generation World-Leading Researches (NEXT Program)" initiated by the Council for Science and Technology Policy, by Shiseido Female Researcher Science Grant, Uehara Memorial Foundation, Okayama Medical Foundation, Suzuken Memorial Foundation and by a Takeda Science Foundation grant to Y.K.

Author contributions

Y.K. planned and designed the study, performed the experiments, and wrote the paper. K.I., Y.U., S.T., K.N., M.K., A.S., T.T., K.K., and S.M. carried out the experiments and analysed data. K.N. gave conceptual advice.

Additional information

Supplementary Information accompanies this paper at http://www.nature.com/naturecommunications

Competing financial interests: The authors declare no competing financial interests.

Reprints and permission information is available online at http://npg.nature.com/reprintsandpermissions/

How to cite this article: Katanosaka, Y. *et al.* TRPV2 is critical for the maintenance of cardiac structure and function in mice. *Nat. Commun.* 5:3932 doi: 10.1038/ncomms4932 (2014).

Neurobiology of Disease

The Role of Pak-Interacting Exchange Factor-β Phosphorylation at Serines 340 and 583 by PKCγ in Dopamine Release

Toshihiko Shirafuji,[1] Takehiko Ueyama,[1] Ken-ichi Yoshino,[1] Hideyuki Takahashi,[1] Naoko Adachi,[1] Yukio Ago,[2] Ken Koda,[2] Tetsuaki Nashida,[2] Naoki Hiramatsu,[2] Toshio Matsuda,[2] Tatsushi Toda,[3] Norio Sakai,[4] and Naoaki Saito[1]

[1]Laboratory of Molecular Pharmacology, Biosignal Research Center, Kobe University, Kobe 657-8501, Japan, [2]Laboratory of Medicinal Pharmacology, Graduate School of Pharmaceutical Sciences, Osaka University, Suita, Osaka 565-0871, Japan, [3]Division of Neurology/Molecular Brain Science, Kobe University Graduate School of Medicine, Kobe 650-0017, Japan, and [4]Department of Molecular and Pharmacological Neuroscience, Graduate School of Biomedical Sciences, Hiroshima University, Hiroshima 734-8551, Japan

Protein kinase C (PKC) has been implicated in the control of neurotransmitter release. The AS/AGU rat, which has a nonsense mutation in PKCγ, shows symptoms of parkinsonian syndrome, including dopamine release impairments in the striatum. Here, we found that the AS/AGU rat is PKCγ-knock-out (KO) and that PKCγ-KO mice showed parkinsonian syndrome. However, the PKCγ substrates responsible for the regulated exocytosis of dopamine *in vivo* have not yet been elucidated. To identify the PKCγ substrates involved in dopamine release, we used PKCγ-KO mice and a phosphoproteome analysis. We found 10 candidate phosphoproteins that had decreased phosphorylation levels in the striatum of PKCγ-KO mice. We focused on Pak-interacting exchange factor-β (βPIX), a Cdc42/Rac1 guanine nucleotide exchange factor, and found that PKCγ directly phosphorylates βPIX at Ser583 and indirectly at Ser340 in cells. Furthermore, we found that PKC phosphorylated βPIX *in vivo*. Classical PKC inhibitors and βPIX knock-down (KD) significantly suppressed Ca^{2+}-evoked dopamine release in PC12 cells. Wild-type βPIX, and not the βPIX mutants Ser340 Ala or Ser583 Ala, fully rescued the decreased dopamine release by βPIX KD. Double KD of Cdc42 and Rac1 decreased dopamine release from PC12 cells. These findings indicate that the phosphorylation of βPIX at Ser340 and Ser583 has pivotal roles in Ca^{2+}-evoked dopamine release in the striatum. Therefore, we propose that PKCγ positively modulates dopamine release through β2PIX phosphorylation. The PKCγ-βPIX-Cdc42/Rac1 phosphorylation axis may provide a new therapeutic target for the treatment of parkinsonian syndrome.

Key words: βPIX; Cdc42; dopamine; Parkinson's disease; phosphoproteome; PKC

Introduction

Protein kinase C (PKC) is an important kinase in the enhancement of Ca^{2+}-triggered exocytosis (Iwasaki et al., 2000; Barclay et al., 2003). The PKC family consists of at least 10 subtypes and is divided into the following three subfamilies: conventional PKC (cPKC), novel PKC, and atypical PKC (Nishizuka, 1988, 1992). Among PKCs, only cPKCs (including PKCγ, which is a neuron-specific PKC isoform; Saito and Shirai, 2002) are activated by Ca^{2+} because they contain a C2 domain that specifically binds to Ca^{2+} and phosphatidylserine (PS; Murray and Honig, 2002).

Received Oct. 6, 2013; revised May 18, 2014; accepted May 29, 2014.

Author contributions: N. Saito designed research; T.S., H.T., N.A., Y.A., K.K., T.N., and N.H. performed research; K.Y. contributed unpublished reagents/analytic tools; T.U., T.M., T.T., N. Sakai, and N. Saito analyzed data; T.S., T.U., and N. Saito wrote the paper.

We thank Sumio Sugano (University of Tokyo) and Yoshihide Hayashizaki (RIKEN Omics Science Center and Research Association for Biotechnology) for kindly providing the βPIX cDNA and Hiroshi Kiyonari and Kazuki Nakao (RIKEN CDB) for mice preservation.

The authors declare no competing financial interests.

Correspondence should be addressed to Naoaki Saito, 1-1 Rokkodai-cho, Nada-ku, Kobe 657-8501 Japan. E-mail: naosaito@kobe-u.ac.jp.

DOI:10.1523/JNEUROSCI.4278-13.2014

 0270-6474/14/349268-13$15.00/0

The AS/AGU rat, a spontaneously occurring mutated animal that exhibits locomotor abnormalities, progressive dopaminergic (DAergic) neuronal degeneration in the substantia nigra (SN), and lower extracellular levels of dopamine (DA) in the striatum, has been used as a valuable model for parkinsonian syndrome (Payne et al., 2000). It is noteworthy that a mutation in PKCγ that leads to the early termination at the C2 domain without possessing the catalytic domain causes parkinsonian syndrome in AS/AGU rats (Craig et al., 2001). The mutation in AS/AGU rats should result in the kinase-dead form of PKCγ, but it is still unclear how the mutation causes parkinsonian symptoms.

PKC has been shown to modify exocytosis in at least three steps: (1) increased vesicle recruitment into readily releasable pools (Gillis et al., 1996; Stevens and Sullivan, 1998), (2) acceleration of fusion pore expansion (Scepek et al., 1998), and (3) changes in the kinetics of exocytosis (Graham et al., 2002). However, only the functional consequences of the phosphorylation of SNAP25 (Iwasaki et al., 2000), synaptotagmin I (Hilfiker et al., 1999), and Munc18 (Barclay et al., 2003) by PKC have been established on exocytosis *in vivo*. Furthermore, no attempts have been made to achieve a comprehensive understanding of DA exocytosis through an identification of

PKCγ substrates. Therefore, we attempted to identify the PKC substrates involved in exocytosis to reveal the mechanisms of regulated exocytosis.

Pak-interacting exchange factor-β (βPIX) is a Rho guanine nucleotide exchange factor (GEF) that specifically activates Rac1 and Cdc42 (Shin et al., 2002; Shin et al., 2004; Chahdi et al., 2005; Feng et al., 2006; Shin et al., 2006; ten Klooster et al., 2006; Chahdi and Sorokin, 2008). βPIX has been reported to be an essential element of the exocytotic machinery in neuroendocrine cells (Audebert et al., 2004; Momboisse et al., 2009). To date, there have been several studies on βPIX phosphorylation (Shin et al., 2002; Chahdi et al., 2005; Shin et al., 2006; Mayhew et al., 2007), but there have been no reports of the involvement of βPIX phosphorylation in DA release.

In the present study, we found that the AS/AGU rat is indeed a PKCγ-knock-out (KO) animal, and our phosphoproteome analysis using PKCγ KO mice found 10 candidates in the striatum that are phosphorylated by PKCγ. Among the 10 candidates, we demonstrated that PKCγ activated DA release through the phosphorylation of βPIX.

Materials and Methods

Antibodies. The anti-GFP antibody (Ab) and the anti-vesicular monoamine transporter 2 (VMAT2) Ab recognizing the C-terminal of mouse VMAT2 were prepared in house. The anti-PKCγ (C2-domain) monoclonal Abs specifically recognizing C2-domain of PKCγ have been described previously (Kose et al., 1990). The following Abs were purchased: anti-FLAG from Sigma-Aldrich (catalog #P2983 RRID:AB_439685); anti-βPIX (SH3 domain) from Millipore; anti-β-actin (catalog #ab66338 RRID:AB_2289239) and anti-PKCγ (N-terminal) specifically recognizing N-terminal of PKCγ from Abcam; anti-glutathione S-transferase (GST) (catalog #sc-33613 RRID:AB_647588), anti-PKCα (catalog #sc-208 RRID:AB_2168668), anti-PKCβ1 (catalog #sc-209 RRID:AB_2168968), anti-PKCβ2 (catalog #sc-210 RRID:AB_2252825), and anti-PKCγ (catalog #sc-211 RRID:AB_632234) from Santa Cruz Biotechnology; and anti-serPKC motif (catalog #2261S RRID: AB_330310), anti-βPIX (catalog #4515S RRID:AB_2274365) for immunoprecipitation (IP), and anti-postsynaptic density-95 (PSD95; catalog #2507S RRID:AB_10695259) from Cell Signaling Technology.

Production of anti-phosphoThr76, anti-phosphoSer340, anti-phosphoSer583, and anti-β2PIX Abs. The production of anti-phospho Abs was performed as described previously (Matsubara et al., 2012). For the preparation of anti-phospho-Thr76 (pT76), anti-phospho-Ser340 (pS340), and anti-phospho-Ser583 (pS583) βPIX Abs, oligopeptides corresponding to the amino acids of human βPIX containing pT76 [VSPKSG(pT)LKSPP], pS340 [SASPRM(pS)GFIYQ], and pS583 [SLGRRS(pS)LSRLE] were used as antigens, respectively. After the fifth boost, serum was collected and purified with an affinity column and the non-phospho-antigen peptide. The anti-β2PIX Ab was obtained by eluting the IgG from those that were bound to the nonphospho-Ser583 peptide column.

Animals. The AS/AGU rats were provided by R.W. Davies (Payne et al., 2000). The PKCγ-Cre knockin (KI) mouse was provided by Z.F. Chen (Ding et al., 2005). After the sixth backcross, homozygous littermates obtained by crossing the heterozygous PKCγ-Cre KI mouse were used as the PKCγ KO and wild-type (WT) mice in the studies. All animal studies were approved by the Institutional Animal Care and Use Committee and conducted according to the Kobe University Animal Experimentation Regulations.

Sample preparation and Western blot analysis. The brains from AS/AGU rats and mice were homogenized and the concentrations of the proteins were measured with a bicinchoninic acid (BCA) protein assay kit (Thermo Fisher Scientific). SDS-PAGE and immunoblot analyses were performed as described previously (Adachi et al., 2005).

Preparation of P2 synaptosomal fraction. Adult male mouse brains were collected and homogenized in ice-cold 0.32 M sucrose solution containing 1 mM phenylmethylsulfonyl fluoride, 20 μg/ml leupeptin, and a phosphatase-inhibitor cocktail (Nacalai Tesque). The total homogenate was subjected to centrifugation at 800 × *g* for 12 min at 4°C to remove the nuclei and the supernatant, which we defined as the total fraction, was further centrifuged at high speed at 22,000 × *g* for 20 min at 4°C. The pellet was used as the P2 synaptosomal fraction. To determine the efficiency of the P2 synaptosomal extraction process, we compared the amount of VMAT2 and PSD95 proteins between the total fraction and P2 synaptosomal fraction in the same amount of protein (50 μg), which was calculated using the BCA protein assay kit.

In vivo *microdialysis. In vivo* microdialysis was performed with male mice essentially as described previously (Koda et al., 2010; Ago et al., 2013). In brief, mice were anesthetized by injection of sodium pentobarbital (40 mg/kg, i.p.), and a guide cannula (one site per animal) for a dialysis probe (Eicom) was implanted stereotaxically in the dorsal striatum (anterior 0.1 mm, lateral 1.8 mm, ventral 2.2 mm relative to the bregma and skull; Franklin and Paxinos, 1997). The cannula was cemented in place with dental acrylic and the animals were maintained warm and allowed to recover from anesthesia. The active probe membrane was 1 mm in length. Two days after the surgery, the probe was perfused with Ringer's solution (147.2 mM NaCl, 4.0 mM KCl, and 2.2 mM $CaCl_2$, pH 6.0; Fuso Pharmaceutical Industries) at a constant flow rate of 1 μl/min. To prepare the Ringer's solution containing 100 mM K^+, an identical amount of sodium was replaced for maintaining isoosmolarity. Experiments were initiated after a stabilization period of 3 h. Microdialysis samples (20 μl) were collected every 20 min and were assayed for DA by high-performance liquid chromatography (HPLC) with electrochemical detection. No-net-flux microdialysis experiments were conducted in a PKCγ KO and WT mice as described previously (Justice, 1993; Chefer et al., 2005; Hewett et al., 2010). Three different concentrations of DA in Ringer's solution (C_{in} of 0, 5 and 20 nM DA) were perfused through the probe and DA in the perfusates (C_{out}) was measured in the fifth fraction following 4 fractions (equilibration period) at each applied DA concentration. A slope was calculated for the linear regression for DA applied (C_{in}) and the difference between dopamine applied and DA measured ($C_{in} - C_{out}$). The slope (extraction fraction) is an indirect measure of dopamine transporter (DAT) dynamics *in vivo* to remove extracellular DA.

Measurement of DA and DA metabolite levels in striatum. The concentrations of DA were quantified by HPLC with an electrochemical detector (ECD-100; Eicom; Kawasaki et al., 2006; Kawasaki et al., 2007). Tissue samples were homogenized in 0.2 M perchloric acid containing 100 μM EDTA and isoproterenol as an internal standard. The homogenate was centrifuged at 15,000 × *g* for 15 min at 0°C. The supernatant was filtered through a 0.22 μm membrane filter (Millipore), and then a 10 μl aliquot of the sample was injected onto the HPLC column every 30 min for the DA assay. An Eicompak SC-5ODS column (3.0 mm i.d. × 150 mm; Eicom) was used, and the potential of the graphite electrode (Eicom) was set to +750 mV against an Ag/AgCl reference electrode. The mobile phase contained 0.1 M sodium acetate/0.1 M citrate buffer, pH 3.5, 190 mg/L octanesulfonic acid, 5 mg/L EDTA, and 17% (v/v) methanol. Data were calculated by analyzing the peak area of the external standard of dopamine hydrochloride (Sigma-Aldrich).

Cell culture. COS7 and HEK293 cells were cultured in DMEM and Eagle's minimum essential medium (Nacalai Tesque), respectively, which were supplemented with 10% fetal bovine serum, penicillin (100 units/ml), and streptomycin (100 μg/ml). Nonessential amino acids (100 μM) were added for HEK293 cells. PC12 cells were cultured in DMEM containing 10% fetal bovine serum and 5% horse serum. All cells were cultured at 37°C in a humidified atmosphere containing 5% CO_2.

Construction of plasmids. WT PKCγ was cloned into pcDNA3.1 (Life Technologies) and the subdomains of PKCγ were cloned into pcDNA3.1 with GFP, as described previously (Seki et al., 2005). Human βPIX was provided by the RIKEN BioResource Center through the National BioResource Project of MEXT in Ibaraki, Japan (Ota et al., 2004). For the construction of plasmids encoding full-length β2PIX that was fused with 3xFLAG at the N terminal, β2PIX with a NotI/BamHI site that was produced by PCR was cloned into a 3xpFLAG-CMV10 vector (Sigma-Aldrich). Because the target sequence for rat βPIX knock-down (KD; sh369) was located in the coding region of βPIX, sh369-resistant β2PIX in the 3xpFLAG-CMV10 vector was made by placing 6-base silent

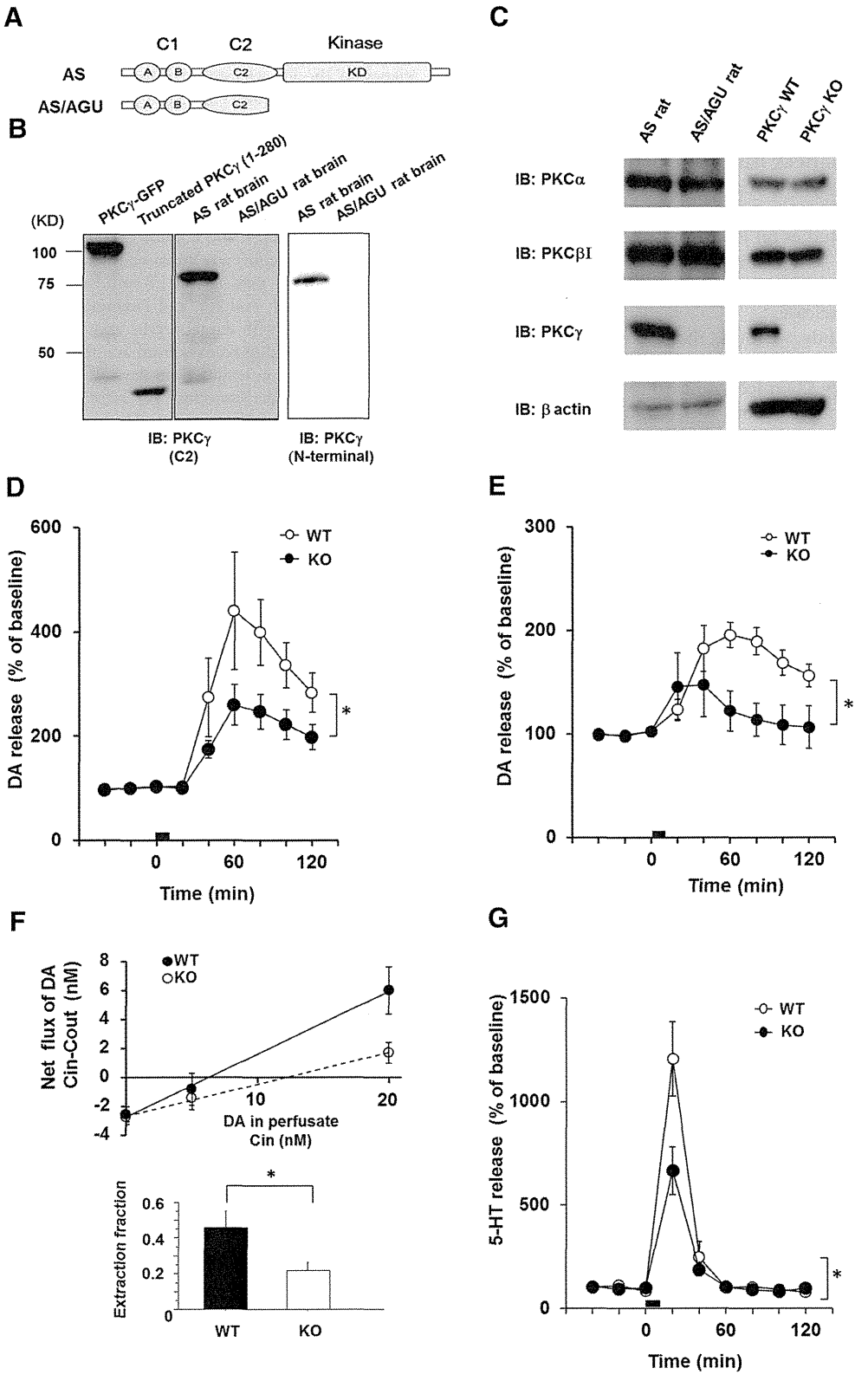

Figure 1. The PKCγ KO model exhibits symptoms of parkinsonian syndrome. ***A***, Schematic illustrations of the PKCγ protein and AS/AGU mutations. The truncated PKCγ polypeptide terminates within the C2 domain. ***B***, Recombinant truncated PKCγ (1–280 aa), which was transfected in COS-7 cells, the AS rat brain lysate, and the AS/AGU rat brain lysate, was detected by immunoblot analysis with an anti-PKCγ (C2-domain) monoclonal antibody and anti-PKCγ (N terminal) antibody, respectively. ***C***, The PKCγ KO was confirmed by immunoblot analysis of the whole brain of the AS/AGU rats and PKCγ KO mice. Arrowheads are recombinant PKCγ-GFP and PKCγ (1–280aa)-GFP, which were used as positive controls. ***D***, *In vivo* microdialysis in the striatum of the PKCγ KO mice. A high level of K^+ was perfused into the striatum through a dialysis probe for the time indicated by the square at 3–4 months. The results are expressed as mean ± SEM ($n = 4–5$, interaction of the genotype and time for DA release that was stimulated by high K^+ levels; $^*p < 0.05$, $F_{(8,48)} = 2.31$, repeated two-way ANOVA). ***E***, *In vivo* microdialysis for DA in the striatum of the PKCγ-KO (KO) mice that were stimulated with METH. METH (1 mg/kg) was perfused into the striatum through a dialysis probe for the time indicated by the square at 3 months (*Figure legend continues.*)

changes within the targeting sequence (5′-CAaACgAGtGAaAAaTTa-3′) with a QuikChange Multisite-Directed Mutagenesis Kit (Agilent Technologies). For construction of plasmids encoding full-length β2PIX or fragments that were fused to GST, full-length β2PIX and the SH3 (1–92 aa), DH (93–274 aa), and PH (275–400 aa) C-terminal (401–625 aa) regions were amplified by PCR with a Not1/BamH1 site and cloned into the pGEX-6P1 vector. Substitutions of Ser or Thr to Ala or Glu at the identified phosphorylation sites (Thr76Ala, Ser215Ala, Ser340Ala or Glu, and Ser583Ala or Glu) were introduced with a QuikChange kit.

Protein expression. Protein expression was performed as described previously (Kawasaki et al., 2010). In brief, BL21 pLys *Escherichia coli* and Sf9 cells were transformed with expression plasmids. *E. coli* and Sf9 cells were harvested and lysed. For the purification of recombinant proteins, GST-fusion proteins were purified with glutathione-Sepharose 4B resin (GE Healthcare Biosciences).

RNAi: short hairpin RNA and small interfering RNA. Double-stranded oligonucleotides were cloned into the short hairpin RNA (shRNA) expression vector, pSuper (puro; Oligoengine). The target sequence for the shRNA rat βPIX KD was 5′-GCAGACCAGCGAGAAGTTGAG-3′ (sh369; cording nucleotides 369–389). Because the βPIX shRNA sequence that we used was common to both the β1 and β2 isoforms, KDs of both β1 and β2 in PC12 cells were examined with βPIX SH3- and β2-specific antibodies. The synthesized small interfering RNA (siRNA) for rat βPIX was composed of a mixture of 4 oligonucleotides (si878: 5′-GGGAUGACAUAAAGACGUU-3′, si806: 5′-AGUGUCAAGAAGU ACGAAA-3′, si1115: 5′-GGAGCAUGAUCGAGCGCAU-3′, and si1153: 5′-CAACAGGACUUGCACGAAU-3′) was purchased from Thermo Fisher Scientific (SmartPool). Verified shRNA plasmids for KD of Cdc42 (sh197; 5′-GATTACGACCGCTGAGTTA-3′; Ueyama et al., 2014) and Rac1 (sh618; 5′-CCTTTGTACGCTTTGCTCA-3′; Ueyama et al., 2006) were described previously.

In vitro *PKC phosphorylation assay.* An *in vitro* PKC phosphorylation assay was performed as described previously (Kawasaki et al., 2010). In brief, precipitated FLAG-tagged β2PIX proteins or purified GST-tagged β2PIX were incubated with 200 ng of GST-tagged PKCγ or GST and the following buffers: 20 mM Tris, pH 7.4, 0.5 mM $CaCl_2$, 10 μM ATP, 0.5 mCi [γ-^{32}P] ATP, 8 μg/ml PS, and 0.8 μg/ml (±)-1,2-didecanoylglycerol (DO) in a 50 μl final volume. The samples were incubated with or without PKC inhibitors, including GF109203X (GFX), which was used as a pan PKC inhibitor, and Gö6976, which was used as a cPKC inhibitor, at 30°C for 15 min. For the calculation of the relative phosphorylation levels, the densitometries of the autoradiography were normalized with the total protein levels. The average relative phosphorylation levels of PKCγ stimulation were defined as 1.00.

PKC phosphorylation assay in cells. A PKC phosphorylation assay in cells was performed as described previously (Kawasaki et al., 2010) but with slight modifications. In brief, HEK293 cells were transfected with WT β2PIX in 3xpFLAG-CMV10 with a NEPA21 electroporator (Nepa Gene). After 12-O-tetradecanoylphorbol 13-acetate (TPA) stimulation with or without PKC inhibitors for 30 min in HEPES buffer at 37°C, the cells were collected and resuspended in homogenization buffer containing 150 mM NaCl, 10 mM ethylene glycol tetraacetic acid, 2 mM ethylenediamine tetracetic acid, 10 mM HEPES, pH 7.4, 1 mM phenylmethylsulfonyl fluoride, 20 μg/ml leupeptin, and a phosphatase-inhibitor cocktail. The precipitated proteins were separated by SDS-PAGE. The phosphorylated proteins were visualized with phospho-Abs. For the calculation of the relative phosphorylation levels, the densitometries of the immunoblots of the phospho-Abs were normalized to the total protein levels in each experiment and the averages of the relative levels of phosphorylation in more than three independent experiments are presented. The phosphorylation levels of the prestimulations were defined as 1.00.

PKC phosphorylation assay in vivo. The mice P2 synaptosomal fraction was resuspended in HEPES buffer containing 1 mM phenylmethylsulfonyl fluoride, 20 μg/ml leupeptin, and a phosphatase-inhibitor mixture and used for the *in vivo* PKC phosphorylation assay (Wu et al., 1982). After 2 μM TPA stimulation with or without 2 μM GFX for 30 min in HEPES buffer at 37°C, the P2 fraction was collected and resuspended in homogenization buffer containing 150 mM NaCl, 10 mM ethylene glycol tetraacetic acid, 2 mM ethylenediamine tetracetic acid, 10 mM HEPES, pH 7.4, 1 mM phenylmethylsulfonyl fluoride, 20 μg/ml leupeptin, and the phosphatase-inhibitor mixture. The precipitated proteins were separated by SDS-PAGE. The phosphorylated proteins were visualized with ser-PKC motif Abs.

DA release assay. DA release assays in βPIX KD cells were performed 96 h after transfection by NEPA21. PC12 cells were washed thrice with 500 μl of incubation solution (140 mM NaCl, 5 mM KCl, 2 mM $CaCl_2$, 1 mM $MgCl_2$, 2 mM glucose, 20 μM pargyline, and 10 mM HEPES, pH 7.5) and then incubated for 60 min in 500 μl of incubation solution with ^{3}H-DA (PerkinElmer), followed by three washes with 500 μl of incubation solution. The cells were allowed to rest or were stimulated with 500 μl of a high-K^+ solution containing 100 mM KCl and 35 mM NaCl for 10 min. The supernatant was collected and the cells were harvested in 500 μl of incubation solution with 2% Triton X-100. The amount of DA that was secreted into the medium and retained in the cells was measured in 500 μl of samples with a scintillation counter LS-6500 (Beckman Coulter). DA secretion was expressed by the following formula: %DA = (^{3}H in supernatant)/(^{3}H in supernatant + ^{3}H in cell lysate). A collagen-IV-coated six-well plate (BD Biosciences) was used for the DA release assay.

Mass spectrometry for β2PIX-phosphorylation site identification. Mass spectrometry for β2PIX-phosphorylation site identification was performed as described previously (Sakuma et al., 2012). After the *in vitro* PKC phosphorylation assay and electrophoresis, silver-stained bands that corresponded to GST-tagged β2PIX proteins were excised and destained. After reduction-alkylation reactions, the proteins in the gels were digested with porcine trypsin (sequencing grade; Promega) in 50 mM ammonium bicarbonate for 15 h at 37°C. The peptide fragments extracted from the gels were subjected to liquid chromatography/tandem mass spectrometry (LC/MS/MS) with a high-performance liquid chromatography system (Paradigm MS4; Michrom Bioresources) coupled to a linear ion trap mass spectrometer (Finnigan LTQ Orbitrap XL; Thermo Fisher Scientific). The LC/MS/MS data were interpreted with a MASCOT MS/MS ions search (Matrix Science).

Phosphoproteome analysis. Phosphoproteome analysis was performed as described previously with some modifications (Saito et al., 2006). Mice striata were dissolved in 50 mM Tris HCl, pH 9.0, 8 M urea, 10 mM ethylenediamine tetracetic acid, 1 mM phenylmethylsulfonyl fluoride, 20 μg/ml leupeptin, and a phosphatase inhibitor mixture. After homogenization with a Dounce homogenizer (10 strokes), the resultant solution was centrifuged at 2000 × *g* for 5 min and the supernatant was collected. The protein amounts were measured with a BCA protein assay kit. The proteins from the striatum were dried and resuspended in 50 mM Tris HCl buffer, pH 9.0, containing 8 M urea at a concentration of 10 μg/μl. These mixtures were subsequently reduced with dithiothreitol, alkylated with acrylamide, and digested with Lys-C endopeptidase at 37°C overnight, followed by trypsin digestion at 37°C overnight. The digested solutions were desalted and concentrated with Empore high-performance extraction disk cartridges (3M). Phosphopeptide enrichment was performed with hydroxy acid-modified metal oxide chromatography (HAMMOC; Titansphere Phos-TiO Kit; GL Sciences; Kyono et al., 2008). For elution of the phosphopeptides, 50 μl of 5% NH_3 and 5% pyrrolidine were used. The fractions were immediately acidified and desalted with SPE-C tips (GL Sciences). A Tomy CC-105 vacuum evap-

←

(*Figure legend continued.*) ($n = 4$, interaction of the genotype and time for DA release stimulated by METH, $F_{(8,48)} = 3.37$; $^*p < 0.01$, repeated two-way ANOVA). ***F***, No-net flux microdialysis to quantitate basal DAT activity in PKCγ KO mice. Three different concentrations of DA in CSF (0, 5, and 20 nM DA) were perfused through the probes to determine the extracellular DA concentration and extraction fraction. Linear regression for the DA perfused and DA measured provided extraction fraction (slope) as an indirect measure of DAT activity *in vivo* to remove extracellular DA. Extraction fraction for WT and KO mice are shown. Data represent mean ± SEM ($n = 4$ and 5 for WT and KO mice, respectively, $^*p < 0.05$). ***G***, *In vivo* microdialysis of serotonin in the striatum of the PKCγ-KO mice that were stimulated by high K^+ levels. K^+ (100 mM) was perfused into the striatum through a dialysis probe for the time indicated by the square at 3–4 months. The results are expressed as mean ± SEM ($n = 4$, interaction of the genotype and time for serotonin release that was stimulated by high K^+ levels, $F_{(8,48)} = 5.399$; $^*p < 0.001$, repeated two-way ANOVA).

Table 1. DA and DA metabolite levels in the striatum of PKCγ WT and KO mice

Age (mo)	Genotype	DA (ng/g weight)	DOPAC (ng/g weight)	HVA (ng/g weight)
3	KO	19629.5 ± 625.4	1838.6 ± 68.9	1490.6 ± 89.0
	WT	19516.4 ± 361.1	1999.1 ± 103.4	1652.1 ± 18.4
6	KO	20667.2 ± 803.5	1671.2 ± 113.0	1620.0 ± 93.9
	WT	17416.8 ± 781.3	1559.2 ± 77.2	1334.6 ± 63.7
12	KO	28911.0 ± 1801.4	2576.0 ± 277.9	2378.1 ± 161.3
	WT	29564.9 ± 2581.4	2253.1 ± 202.2	2392.2 ± 128.4

Results are expressed as mean ± SEM of 4–5 mice.
HVA, Homovanillic acid.

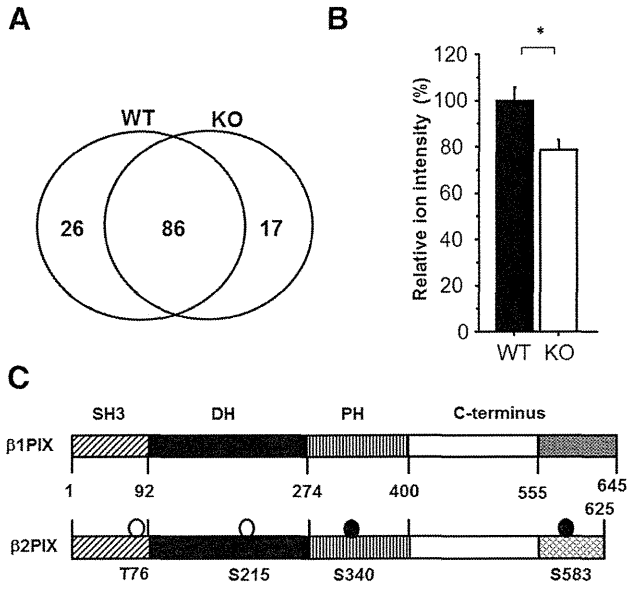

Figure 2. Phosphoproteome analysis revealed 10 phosphopeptides with decreased average ion intensity in PKCγ KO mice striatum. ***A***, Overview of the phosphoproteome (WT, $n = 5$; KO, $n = 4$). ***B***, Average ion intensity of the Ser340 βPIX phosphopeptide is calculated in both PKCγ KO and WT mice ($n = 4–5$; $^*p < 0.05$, unpaired t test). The relative average ion intensity of WT mice was defined as 100%. The results are expressed as mean ± SEM. ***C***, Schematic illustrations of the β1 and β2 PIX protein. The phosphorylation sites that were determined by the *in vitro* PKC phosphorylation assay and the phosphoproteome analysis are circled. The open circles are the phosphorylation sites that were determined only *in vitro*. The closed circles are the phosphorylation sites that were determined *in vitro* and *in vivo*.

orator was used to concentrate the sample and the phosphopeptides were analyzed by LC/MS/MS.

Statistical analysis. The data are presented as mean ± SEM and were analyzed with unpaired t tests, one-way ANOVA with a *post hoc* Dunnett's test, or a repeated two-way ANOVA. The statistical analyses were performed with the Statview 5.0J software package (SAS Institute). p-values of 5% or less were considered statistically significant.

Results

PKCγ KO animals exhibited parkinsonian symptoms, including DA release impairment in the striatum

AS/AGU rats show altered behaviors (Craig et al., 2001), DA release impairment, and the pathology of the nigrostriatal system resembles the pathology observed in human patients with parkinsonian syndrome (Campbell et al., 1996; Payne et al., 2000). AS/AGU rats have a spontaneously occurring mutation that changes the CAG (Glu281) codon to a TAG (stop codon) in PKCγ, and the putatively truncated PKCγ, if produced, will terminate at the fifth residue from the C terminus of the last strand of the β-sheet structure of the C2 domain (Fig. 1*A*). The truncated protein may result in a severe or complete loss of the kinase function of PKCγ, although it has not yet been clarified whether the truncated protein is expressed in AS/AGU rats. Although both anti-PKCγ (N terminal) Ab and anti-PKCγ (C2-domain) Ab detected an 80 kDa single band in AS rats, no band was detected in the AS/AGU rats (Fig. 1*B*). These findings indicated that PKCγ was not expressed in AS/AGU rats, suggesting the hypothesis that PKCγ KO mice show similar symptoms as those observed in AS/AGU rats. We first confirmed that our PKCγ KO mice did not express PKCγ, whereas the expression levels of other members of cPKCs were unaltered (Fig. 1*C*). To determine the effects of the PKCγ KO on DA release in the striatum, we performed *in vivo* microdialysis in the striatum. The basal line extracellular levels of DA in the striatum did not differ significantly between the PKCγ WT and KO mice. After treatment with high levels of K^+ (Fig. 1*D*) and methamphetamine (METH; Fig. 1*E*), the increase in DA release in the WT was significantly larger than that in the KO 3–4 months after birth. Although high K^+ levels induced DA release is mediated by exocytosis and not by DAT, PKC induces DAT endocytosis (Daniels and Amara, 1999), which may decrease the extracellular DA levels by increasing

Table 2. List of phosphopeptides with a PKC phosphorylation motif

Protein name	Accession no.	Sequence	Site	No. of phosphopeptides		Lowest peptide score		Highest peptide score		Average ion intensity		
				WT	KO	WT	KO	WT	KO	WT	KO	WT/KO
Gap junction alpha-1 protein	NP 034418	KVAAGHELQPLAIVDQRPSSRA	S365	7	0	11	—	28	—	3	0.4	7.3
Disks large-associated protein 1	NP 808307	RSLDSLDPAGLLTSPKF	S437	5	0	48	—	77	—	3.4	0.8	4.4
MAP kinase-activating death domain protein	NP 001171190	RATLSDSEIETNSATSAIFGKA	T1235	8	4	40	26	90	58	3.7	1	3.9
DnaJ homolog subfamily C member 5	NP 001258513	RSLSTSGESLYHVLGLDKN	S10	54	55	3	4	88	85	969	299.5	3.2
Calnexin	NP 001103969	KAEEDEILNRSPRN	S582	6	2	25	22	31	34	3.1	1.8	1.8
Stathmin	NP 062615	KRASGQAFELILSPRS	S16	26	23	8	6	93	84	12.1	7.5	1.6
Stathmin	NP 062615	RASGQAFELILSPRS	S25	25	17	5	19	81	83	7.4	5.9	1.3
Rho guanine nucleotide exchange factor 7	NP 001106989	RMSGFIYQGKL	S340	3	0	24	—	59	—	1.8	1.4	1.4
Reticulon-4	NP 077188	RRGSGSVDETLFALPAASEPVIPSSAEKI	S165	15	8	34	41	70	59	2.3	1.7	1.3
α-adducin	NP 001019629	KFRTPSFLKK	S724	3	2	7	9	29	25	6.1	4.8	1.3
β-adducin	NP 001258786	KDIATEKPGSPVKS	S594	10	8	10	17	50	56	0.4	0.3	1.2

Phosphopeptides with a WT/KO ratio >1.0 are listed. The numbers of phosphorylation sites are based on the results of mice in PhosphoSitePlus (www.phosphosite.org). S and T are the identified phosphorylation sites. Number of phosphopeptides means the total numbers of the phosphopeptides in each group ($n = 4$). Highest or lowest peptide score means the highest or lowest peptide score in each group ($n = 4$). Peptides that were not detected are shown as —.

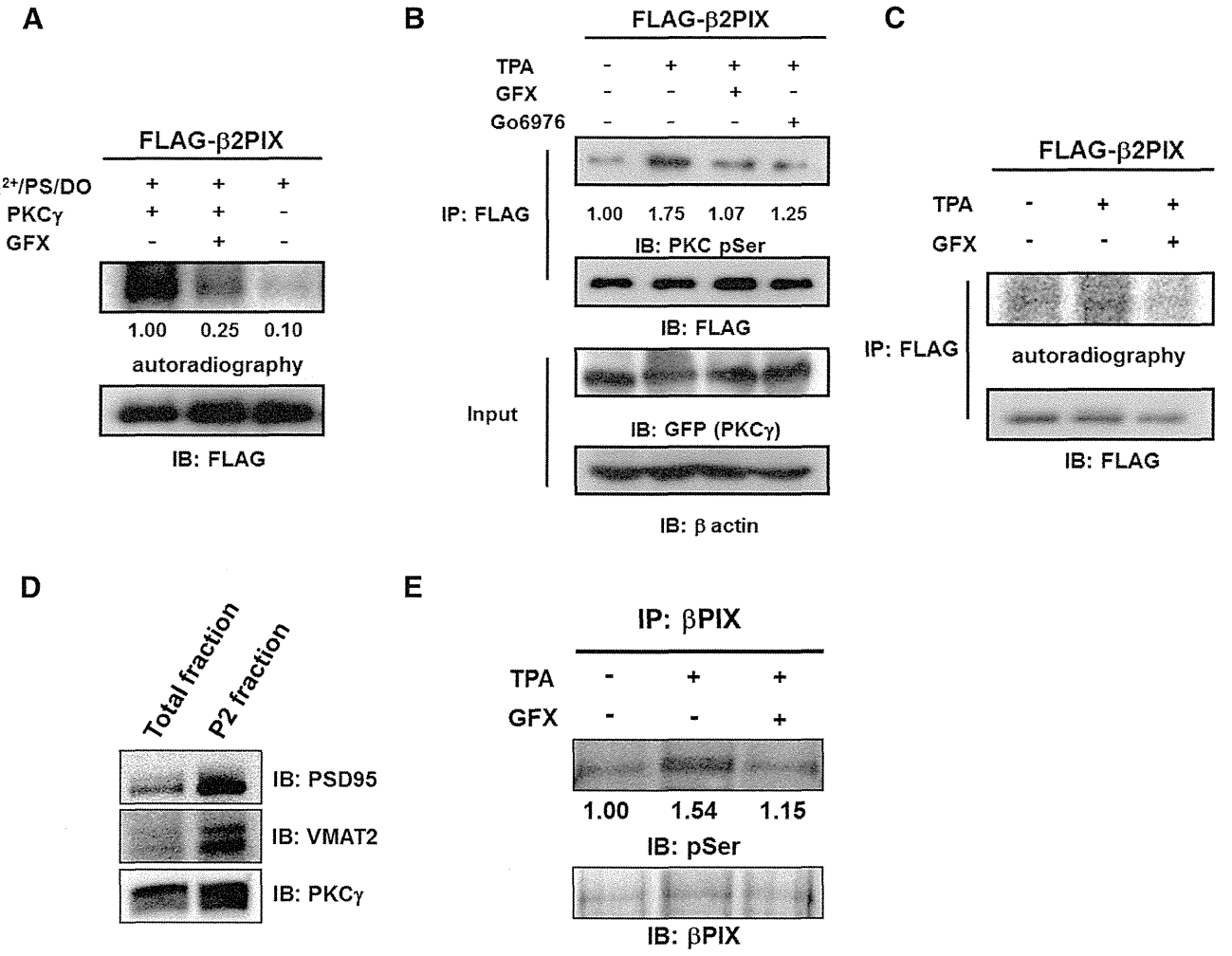

Figure 3. βPIX is phosphorylated by PKCγ *in vitro*, in cells, and *in vivo*. ***A***, *In vitro* phosphorylation of β2PIX. FLAG-tagged β2PIX proteins were purified and incubated with or without recombinant PKCγ in the presence of PKC activator (PS/DO/Ca^{2+}) and [γ-^{32}P] ATP for 20 min. The *in vitro* phosphorylation of β2PIX was also performed in the presence of GFX. The phosphorylated proteins were detected by autoradiography and the levels of protein expression were determined by Western blotting with an anti-FLAG antibody. The numbers show the relative phosphorylation levels that were normalized to PKCγ stimulation as 1.00 ($n = 3$). ***B***, In-cell phosphorylation of β2PIX. HEK293 cells expressing FLAG-tagged β2PIX and GFP-tagged PKCγ were stimulated with 1 μM 12-O-TPA for 20 min in the presence or absence of 1 μM GFX or 1 μM Gö6976. FLAG-tagged β2PIX proteins were purified with anti-FLAG agarose resin. Phosphorylated proteins were detected by an immunoblot analysis with an anti-pSer PKC motif antibody. Protein expression was determined by Western blotting with an anti-FLAG antibody. The average relative phosphorylation levels for each experimental condition were normalized to the prestimulation signal set as 1.00 ($n = 5$). ***C***, PC12 cells expressing FLAG-tagged β2PIX were incubated with ^{32}P monosodium phosphate and stimulated with 1 μM 12-O-TPA in the absence or presence of 1 μM GFX. FLAG-tagged β2PIX proteins were purified with anti-FLAG agarose resin. Phosphorylated proteins were detected by autoradiography, and protein expression was determined by immunoblots with an anti-FLAG antibody. ***D***, The same amount of samples of total fraction and the P2 synaptosomal fraction were immunoblotted by anti-PSD95 antibody as a postsynaptic marker, anti-VMAT2 antibody as a presynaptic marker, and anti-PKCγ antibody. ***E***, the P2 synaptosomal fraction was stimulated with 2 μM 12-O-TPA in the absence or presence of 2 μM GFX. βPIX proteins were purified with anti-βPIX antibody. Phosphorylated proteins were detected by phospho-Abs. The numbers show the relative phosphorylation levels that were normalized to pretreatment as 1.00 ($n = 3$).

DAT activity in PKCγ KO mice striatum. To evaluate the DAT activity in PKCγ KO mice, we performed the no-net-flux microdialysis experiment. The slope (extraction fraction) is the measure of the activity of DAT *in vivo*. Fig. 1*G* shows decreased DAT activity in the striatum of PKCγ KO mice, suggesting that PKCγ KO mice tend to have increased rather than decreased extracellular DA levels compared with WT mice (Fig. 1*F*). Consistent with our results, the increase in the serotonin release stimulated by high K^+ levels in WT was also significantly larger than that of the KO (Fig. 1*G*), as described previously in AS/AGU rats (Al-Fayez et al., 2005). Because we had preliminary data that suggested slight loss of DAergic neurons in 12-month-old, but not 3- or 6-month-old, PKCγ KO mice, there was a possibility that the decrease in DA release in PKCγ KO mice was due to the decrease in DA in the striatum. We measured DA and its metabolites using HPLC in the striatum. No difference in DA or DA metabolite levels in the striatum was observed between PKCγ KO mice and WT mice at 3, 6, and 12 months (Table 1), suggesting that DA release disorder was from the exocytotic machinery disorder instead of the lack of the DAergic neurons in the nigrostriatum system. These results suggested that the PKCγ KO mice would show similar parkinsonian symptoms as those observed in the AS/AGU rats. From the analysis of the PKCγ KO mice and AS/AGU rats, we concluded that PKCγ KO animals could be used as a practical model of parkinsonian syndrome.

Phosphoproteome analysis identified 10 phosphoproteins, including βPIX, with a PKC-phosphorylation motif

We hypothesized that a loss or decrease of PKCγ-mediated phosphorylation in the nigrostriatal system results in DA release im-

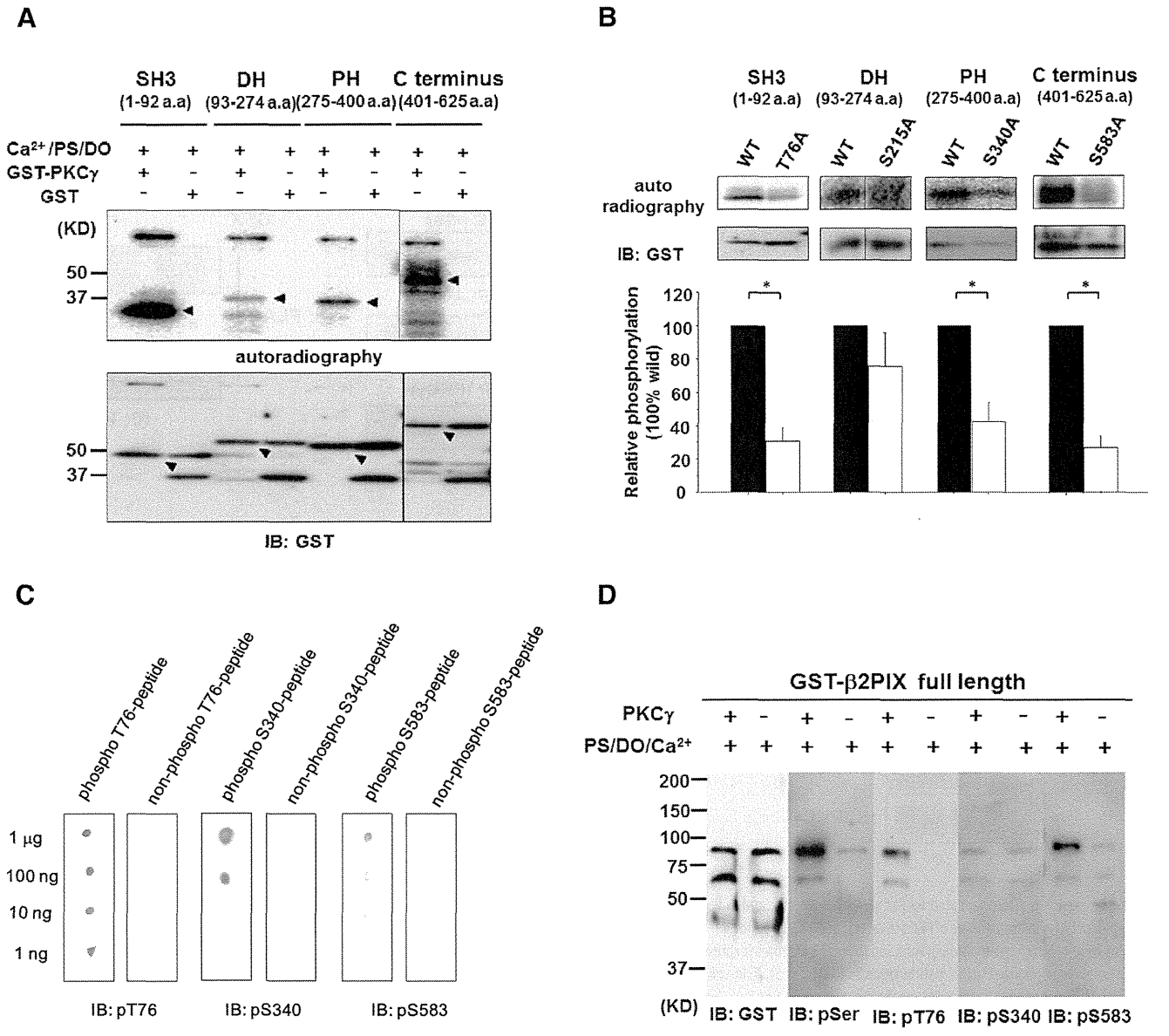

Figure 4. Analysis of the *in vitro* PKCγ phosphorylation sites in β2PIX. ***A***, *In vitro* phosphorylation of the GST-tagged β2PIX SH3, DH, PH, and C terminus regions. Each protein region was expressed in *E. coli*, purified, and incubated with [γ^{32}P] ATP and recombinant PKCγ in the presence of Ca^{2+}, PS, and DO. The phosphorylated proteins were separated by SDS-PAGE and detected by autoradiography (top). The protein levels of the recombinant β2PIX protein regions were detected by Western blotting (bottom). The arrowheads on the top indicate the autoradiography and those on the bottom indicate the total protein for each domain. ***B***, *In vitro* phosphorylation of the β2PIX SH3, DH, PH, and β2 C terminus regions containing the indicated mutations determined by an *in vitro* phosphorylation assay that was followed by mass spectrometry and phosphoproteome analysis. Phosphorylation levels were normalized to the WT phosphorylation signal for each domain, which were set to 100%: SH3 ($n = 5$), DH ($n = 4$), PH ($n = 5$), β2 C terminus ($n = 3$); The results are expressed as mean ± SEM (*$p <$ 0.05, unpaired *t* test). ***C***, Specificity of anti-phospho-Thr76, Ser340, and Ser583 antibodies. The indicated amount of the phospho-peptide (pT76 [VSPKSG(pT)LKSPP], pS340 [SASPRM-(pS)GFIYQ], and pS583 [SLGRRS(pS)LSRLE]) or non-phosphopeptide was dotted on the PVDF membrane. Immunostaining was performed using purified anti-pT76, pS340, and pS583 antibodies. ***D***, *In vitro* phosphorylation assay of full-length β2PIX. GST-tagged full-length β2PIX was expressed in *E. coli*, purified, and incubated with ATP and recombinant PKCγ in the presence of Ca^{2+}, PS, and DO. Phosphorylated proteins were separated by SDS-PAGE and detected by an anti-pSer PKC motif antibody, an anti-pT76 antibody, an anti-pS340 antibody, or an anti-pS583 antibody, respectively.

pairment. To identify the substrates for PKCγ, we performed a phosphoproteome analysis using HAMMOC methods (Kyono et al., 2008; Fig. 2*A*). Among the phosphopeptides in the WT group, we chose the proteins that may have a relationship to exocytosis and then calculated the WT/KO ratio of the average ion intensity. The average ion intensity ratio of the phosphopeptides that included the PKC phosphorylation motif are shown in Table 2. Among these 10 candidates, we focused on βPIX (Fig. 2*B*), even when the degree of the phosphorylation decrease was small, because it is expressed in DAergic neurons in the SNpc (http://www.informatics.jax.org/assay/MGI:4944920) and has been reported to play important roles in the machinery of exocytosis (Audebert et al., 2004; Momboisse et al., 2009). In the present phosphoproteome analysis, phosphorylation of Ser340 in β2PIX was detected. The βPIX family consists of two splicing forms, β1 and β2; the difference between β1 and β2 PIX exists in the C terminus (Fig. 2*C*). Although both β1 and β2 contain Ser340, β2PIX is the predominant form in the CNS (Koh et al., 2001). Therefore, β2PIX was used in the present study.

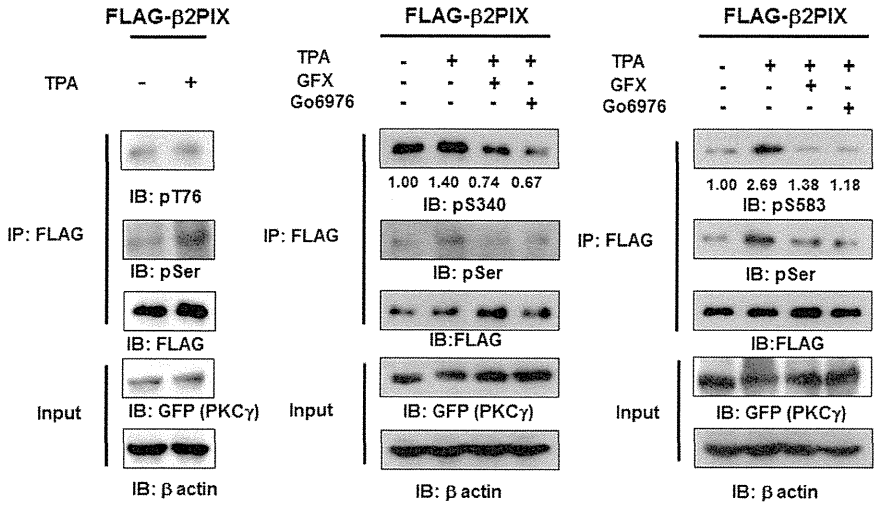

Figure 5. PKC mediates the phosphorylation of full-length β2PIX at Ser340 and Ser583 in cells. HEK293 cells transfected with FLAG-tagged WT β2PIX and GFP-tagged PKCγ were stimulated with 1 μM TPA in the presence or absence of 1 μM GFX, which is a pan-PKC inhibitor, or Gö6976, which is a cPKC inhibitor. FLAG-tagged β2PIX was precipitated and separated by SDS-PAGE. The total amounts of protein were determined by immunoblot analyses with an anti-FLAG antibody. GFP-tagged PKCγ or β actin was detected by anti-GFP or anti-β-actin antibodies. The phosphorylation levels of the FLAG-tagged β2PIX proteins that were determined with an anti-pT76 antibody (***A***; $n = 2$), an anti-pS340 (***B***; $n = 4$), or an anti-pS583 (***C***; $n = 4$) antibody were normalized to the phosphorylation levels of the WT. The numbers show the average relative phosphorylation levels that were normalized to prestimulation levels set as 1.00.

βPIX is phosphorylated by PKCγ *in vitro*, in cells, and *in vivo*

To determine whether β2PIX was phosphorylated by PKCγ, we performed *in vitro*, in cells, and *in vivo* phosphorylation experiments. β2PIX was phosphorylated by PKCγ *in vitro*, whereas the inhibition of PKC activity with GFX abolished the phosphorylation (Fig. 3*A*). Next, we investigated whether β2PIX was phosphorylated by PKC in cells. Enhanced phosphorylation of FLAG-tagged β2PIX extracted from HEK293 cells transfected with FLAG-tagged β2PIX and GFP-tagged PKCγ after treatment with 1 μM TPA was observed with an anti-Ser PKC motif Ab (Fig. 3*B*). Furthermore, the TPA-induced phosphorylation of β2PIX in cells was reduced by the PKC inhibitors Gö6976 and GFX (Fig. 3*B*). These results were further confirmed in PC12 cells (Fig. 3*C*) and in the P2 synaptosomal fraction of the mouse brain (Fig. 3*D*). Collectively, these results showed that β2PIX was phosphorylated by Ca^{2+}-dependent PKC *in vitro*, in cells, and *in vivo*.

PKCγ phosphorylates Thr76 in SH3, Ser340 in PH, and Ser583 in the C terminus of β2PIX *in vitro*

β2PIX consists of the following four regions: SH3 (1–92 aa), DH (93–274 aa), PH (275–400 aa), and the C terminus (401–625 aa). Because each region of β2PIX contains one or more predicted PKC phosphorylation sites, we performed an MS analysis combined with an in vitro phosphorylation assay using full-length GST-tagged β2PIX for screening the phosphorylation sites by PKCγ. The *in vitro* PKC assay, followed by the MS analysis, revealed the phosphorylation of Thr76, Ser215, and Ser583 in addition to that of Ser340, which was revealed by the phosphoproteome analysis of PKCγ KO mice (Fig. 2*C*). Thr76, Ser215, and Ser340 are common sites in both β1 and β2PIX. However, Ser583 is found only in β2PIX. To examine the PKCγ-mediated phosphorylation of these sites, recombinant proteins were used in *in vitro* phosphorylation assays. Importantly, all domains of β2PIX were phosphorylated by PKCγ *in vitro*, but the SH3 and C-terminal domains were phosphorylated much more strongly than the DH and PH domains (Fig. 4*A*). For the next step, we generated recombinant mutant proteins in which each Ser or Thr residue was replaced with Ala (Thr76Ala in SH3, Ser215Ala in DH, Ser340Ala in PH, and Ser583Ala in the C terminus) and examined which Ser/Thr residues of Thr76, Ser215, Ser340, or Ser583 could be phosphorylated by PKCγ *in vitro*. We observed that the Thr76Ala and Ser583Ala mutant proteins exhibited impaired phosphorylation of the SH3 and C-terminal domains (Fig. 4*B*). The Ser340Ala in the PH domain showed a moderately reduced phosphorylation. The Ser215Ala showed no significant reduction of phosphorylation in the DH domain. These findings suggested that Thr76, Ser340, and Ser583, but not Ser215, are PKCγ phosphorylation sites *in vitro*.

cPKC phosphorylates β2PIX Ser340 and Ser583 in cells

To further confirm that β2PIX is phosphorylated by cPKC in cells, we produced Abs that specifically recognized phosphorylated Thr76, Ser340, and Ser583 (Fig. 4*C*). The purified full-length β2PIX was phosphorylated by recombinant PKCγ *in vitro* and then applied to SDS-PAGE, which was followed by Western blotting with the anti-pT76, anti-pS340, and anti-pS583 Abs. The β2PIX that was phosphorylated by PKCγ was detected by anti-pT76 and anti-pS583, but not the anti-pS340 Ab (Fig. 4*D*), suggesting that Ser340 was not a direct PKC phosphorylation site. Next, we investigated whether β2PIX was phosphorylated at Thr76, Ser340, and Ser583 in cells. Figure 5 shows that Ser340 and Ser583, but not Thr76, were phosphorylated in TPA-treated HEK293 cells. Moreover, the PKC-dependent phosphorylation of Ser340 and Ser583 was confirmed with the PKC inhibitors Gö6976 and GFX (Fig. 5). These findings suggested that Ser340 and Ser583 were phosphorylated by cPKC in cells. It is noteworthy that Ser583 was phosphorylated directly, whereas Ser340 was phosphorylated indirectly by PKCγ.

Involvement of cPKC in the regulation of DA release

A ^{3}H-DA release assay in PC12 cells, a cell line in a DAergic neuronal model, was used to study the functional role of PKC and βPIX in the regulation of DA release. PC12 cells expressed endogenous βPIXs and cPKCs, including PKCγ (Fig. 6*A*). To determine the degree of DA release stimulated by K^+, PC12 cells were stimulated with various K^+ concentrations and the DA release was increased in a K^+ concentration-dependent manner (Fig. 6*B*). The functional role of cPKC in the regulation of K^+-induced DA release was monitored with Gö6976 and GFX. These PKC inhibitors significantly decreased the high K^+-stimulated DA release (Fig. 6*C*). It is noted that there were no differences of ^{3}H-DA uptake into the PC12 cells between the control and PKC inhibitor groups (Fig. 6*D*,*E*). Gö6976 and GFX also significantly suppressed the TPA-stimulated DA release (Fig. 6*F*). The activation of PKCγ after K^+-induced depolarization was confirmed by monitoring the translocation of GFP-tagged PKCγ from the cytosol to the plasma membrane in PC12 cells (Fig. 7*A*). These